AGU ADVANCING EARTH AND SPACE SCIENCES

AGU Advances

RESEARCH ARTICLE
10.1029/2024AV001355

Effects of Mesoscale Eddies on Southern Ocean Biogeochemistry

Lydia Keppler[1,2], Yassir A. Eddebbar[1], Sarah T. Gille[1], Nicola Guisewhite[3,4], Matthew R. Mazloff[1], Veronica Tamsitt[3,5], Ariane Verdy[1], and Lynne D. Talley[1]

[1]Scripps Institution of Oceanography, University of California San Diego, La Jolla, CA, USA, [2]Vycarb Inc. Brooklyn, Brooklyn, NY, USA, [3]College of Marine Science, University of South Florida, St Petersburg, FL, USA, [4]Monterey Bay Aquarium Research Institute, Moss Landing, CA, USA, [5]Submarine Scientific LLC, San Francisco, CA, USA

Peer Review The peer review history for this article is available as a PDF in the Supporting Information.

Key Points:

- Cyclonic eddies pump dissolved inorganic carbon and nitrate upward, leading to less oceanic carbon uptake (anticyclones opposite)
- Cyclonic eddies pump low-oxygen water upward (anticyclones opposite), and eddy trapping leads to opposite anomalies at depth
- The net anomalous eddy-induced Southern Ocean carbon uptake is $\sim 0.02 \pm 0.02$ Pg C yr^{-1}, with larger seasonal and regional signals

Supporting Information:

Supporting Information may be found in the online version of this article.

Correspondence to:

L. Keppler,
lydi@vy-carb.com

Citation:

Keppler, L., Eddebbar, Y. A., Gille, S. T., Guisewhite, N., Mazloff, M. R., Tamsitt, V., et al. (2024). Effects of mesoscale eddies on southern ocean biogeochemistry. *AGU Advances*, *5*, e2024AV001355. https://doi.org/10.1029/2024AV001355

Received 13 JUN 2024
Accepted 8 NOV 2024

Author Contributions:

Conceptualization: Lydia Keppler, Yassir A. Eddebbar, Sarah T. Gille, Matthew R. Mazloff, Veronica Tamsitt, Ariane Verdy, Lynne D. Talley
Formal analysis: Lydia Keppler
Investigation: Lydia Keppler
Methodology: Lydia Keppler, Yassir A. Eddebbar, Sarah T. Gille, Matthew R. Mazloff, Veronica Tamsitt, Ariane Verdy, Lynne D. Talley
Validation: Lydia Keppler, Nicola Guisewhite

Abstract The Southern Ocean is rich in highly dynamic mesoscale eddies and substantially modulates global biogeochemical cycles. However, the overall surface and subsurface effects of eddies on the Southern Ocean biogeochemistry have not been quantified observationally at a large scale. Here, we co-locate eddies, identified in the Meta3.2DT satellite altimeter-based product, with biogeochemical Argo floats to determine the effects of eddies on the dissolved inorganic carbon (DIC), nitrate, and dissolved oxygen concentrations in the upper 1,500 m of the ice-free Southern Ocean, as well as the eddy effects on the carbon fluxes in this region. DIC and nitrate concentrations are lower in anticyclonic eddies (AEs) and increased in cyclonic eddies (CEs), while dissolved oxygen anomalies switch signs above (CEs: positive, AEs: negative) and below the mixed layer (CEs: negative, AEs: positive). We attribute these anomalies primarily to eddy pumping (isopycnal heave), as well as eddy trapping for oxygen. Maximum anomalies in all tracers occur at greater depths in the subduction zone north of the Antarctic Circumpolar Current (ACC) compared to the upwelling region in the ACC, reflecting differences in background vertical structures. Eddy effects on air–sea CO_2 exchange have significant seasonal variability, with additional outgassing in CEs in fall (physical process) and additional oceanic uptake in AEs and CEs in spring (biological and physical process). Integrated over the Southern Ocean, AEs contribute $\sim 0.03 \pm 0.01$ Pg C yr^{-1} ($7 \pm 2\%$) to the Southern Ocean carbon uptake, and CEs offset this by $\sim 0.01 \pm 0.01$ Pg C yr^{-1} ($2 \pm 2\%$). These findings underscore the importance of considering eddy impacts in observing networks and climate models.

Plain Language Summary Here, we explore the impacts of swirling currents called mesoscale eddies on various biogeochemical properties of the upper ice-free Southern Ocean. We used data from drifting floats that measure those properties and combined them with data about eddies detected from satellites. We found that eddies changed the dissolved inorganic carbon (DIC), nitrate, and oxygen levels mostly due to a process called eddy pumping, where the eddies push water up or down. Cyclonic eddies, which swirl clockwise in the Southern Hemisphere, tended to bring up deep, nutrient-rich water, increasing DIC and nitrate levels. Anticyclonic eddies, which swirl counterclockwise in the Southern Hemisphere, tended to push waters down, decreasing DIC and nitrate levels. The effects were stronger in certain regions and during specific seasons, with cyclonic eddies mostly causing more carbon dioxide (CO_2) to be released into the atmosphere, while anticyclonic eddies usually led to more CO_2 being absorbed by the ocean. Eddy impacts on oxygen showed a more complex picture, with higher oxygen near the surface and lower oxygen at depth in cyclonic eddies, and vice versa for anticyclones. Our findings emphasize the importance of considering eddies in measurement strategies and climate models.

1. Introduction

The Southern Ocean plays a crucial role in global biogeochemical cycles, substantially modulating the global biological production and the air–sea balance of carbon dioxide (CO_2) and oxygen. Approximately half of the oceanic uptake of anthropogenic carbon from the atmosphere ($\sim 1.8 \pm 0.1$ Pg C yr^{-1} in 2022) occurs in the Southern Ocean (Friedlingstein et al., 2023; Landschützer et al., 2016), and this region is also a major ventilation region, with an air-to-sea oxygen flux of $\sim 183 \pm 80$ Tmol yr^{-1} between 2008 and 2016 (Bushinsky et al., 2017). The Southern Ocean also supplies nutrients to the global thermocline through upwelling and entrainment into Subantarctic Mode Water, aiding global primary production and carbon export (Sarmiento et al., 2004). At the same time, the Southern Ocean is highly variable, with different dominant processes in each of the frontal zones

Writing – original draft: Lydia Keppler
Writing – review & editing: Yassir A. Eddebbar, Sarah T. Gille, Matthew R. Mazloff, Veronica Tamsitt, Ariane Verdy, Lynne D. Talley

and basins and large fluctuations on timescales from subseasonal to decadal (Gray, 2024; Keppler & Landschützer, 2019; Landschützer et al., 2015, 2016; Prend, Keerthi, et al., 2022), adding to the uncertainty in the global oceanic carbon sink (Gruber et al., 2019).

Concurrently, the Southern Ocean is dominated by highly dynamic mesoscale eddies (hereafter referred to as "eddies"), vortices with typical radii ranging from 40 to 150 km and typical lifetimes on the order of months (Chelton et al., 2011). Eddies transport carbon, oxygen, and nutrients, both horizontally and vertically (Dawson et al., 2018; Dufois et al., 2014; Gray, 2024; Patel et al., 2020; Schütte et al., 2016; Su et al., 2021). Four distinct mechanisms that influence this transport have been identified (Figure 1): (i) eddy pumping (isopycnal heaving), (ii) eddy-induced Ekman pumping, (iii) eddy stirring, and (iv) eddy trapping (Beal et al., 2011; Frenger et al., 2015, 2018; Gaube et al., 2014, 2015; Gruber et al., 2011; McGillicuddy, 2016).

Given the pronounced vertical gradients in ocean biogeochemical tracers in this region, we might expect the vertical processes (i and ii) to exert a major influence on ocean biogeochemistry. During *eddy pumping* (Figure 1i), water is shifted upward in cyclonic eddies (CE) and downward in anticyclonic eddies (AE) as a result of isopycnal doming and deepening, respectively (i.e., heaving; McGillicuddy, 2016). Because deeper water tends to be colder and contains lower dissolved oxygen and higher nutrient and dissolved inorganic carbon (DIC) concentrations than surface water, eddy pumping in CEs leads to colder sea surface temperatures (SSTs), and eddy cores with colder temperatures, lower dissolved oxygen, and higher nutrient and DIC concentrations. The inverse is the case for AEs (McGillicuddy, 2016).

During *eddy-induced Ekman pumping* (Figure 1ii and Text S2 in Supporting Information S1), wind forcing modulated by the eddy circulation and temperature gradients can create Ekman convergence or divergence in an eddy, leading to vertical transport (e.g., Gaube et al., 2015; McGillicuddy, 2016; McGillicuddy et al., 2007; Stern, 1965). On average, an eddy-induced curl of Ekman transport leads to Ekman pumping in the opposite direction of the underlying eddy pumping/isopycnal heave, that is, downward pumping in CEs and upward pumping in AEs. Although eddy-induced Ekman pumping is near-surface, tends to be weak, and usually only partially offsets the effects of heaving, it can be significant in regions of strong winds such as the Southern Ocean (Dufois et al., 2014; Liu et al., 2023; Su et al., 2021).

Lateral stirring and trapping (Figures 1iii and 1iv) also play a role in modifying eddy properties, although the vertical processes dominate in our study region. These lateral mechanisms and impacts are described in Text S1 in Supporting Information S1, with additional references.

Any of these processes can lead to indirect biogeochemical feedbacks. For example, increased nutrients at the surface due to eddy-induced upwelling could enhance biological production (Doddridge & Marshall, 2018), leading to increased oxygen and decreased inorganic carbon near the surface due to enhanced photosynthesis but reduced oxygen and increased DIC at depth due to intensified microbial respiration of organic matter (Schütte et al., 2016). Further, different processes dominate in different regions of the Southern Ocean, such as the upwelling of Circumpolar Deep Water near the ACC and subduction near the Antarctic coast and north of the ACC (Talley et al., 2011), shaping regionally distinct background biogeochemical (BGC) gradients against which eddies operate. Moreover, the seasonal cycle is strong in this high-latitude region. Deep mixed layers and limited light in winter, in contrast to shallow mixed layers and more light availability in summer (Sarmiento & Gruber, 2006), could be modulating the seasonality of the eddy effects on BGC. Additionally, variability in the spatial distribution of eddy kinetic energy and eddy size can have a varying influence on the surrounding BGC. Some of these processes have opposing effects, which make it challenging to predict a priori which process will dominate in a region or season.

These eddy-induced BGC anomalies can alter ecosystem habitat structures, which, when superimposed on large-scale variability and long-term change, could drive ecosystem stressors beyond critical thresholds (Köhn et al., 2022). Thus, given long-term strengthening of the amplitude of mesoscale activity (Martínez-Moreno et al., 2022) and an increase in mesoscale eddy kinetic energy (Hogg et al., 2015; Patara et al., 2016), characterizing the effects of mesoscale eddies on the Southern Ocean BGC is crucial for understanding the Southern Ocean's future role in the global carbon cycle and in shaping marine ecosystem habitat change.

Theory and modeling studies have demonstrated that eddies affect the carbon budget. For example, export rates differ at regional scales when eddies are resolved in a global Earth system model (Harrison et al., 2018). In the Southern Ocean, eddies were found to reduce the northward transport of anthropogenic carbon into the

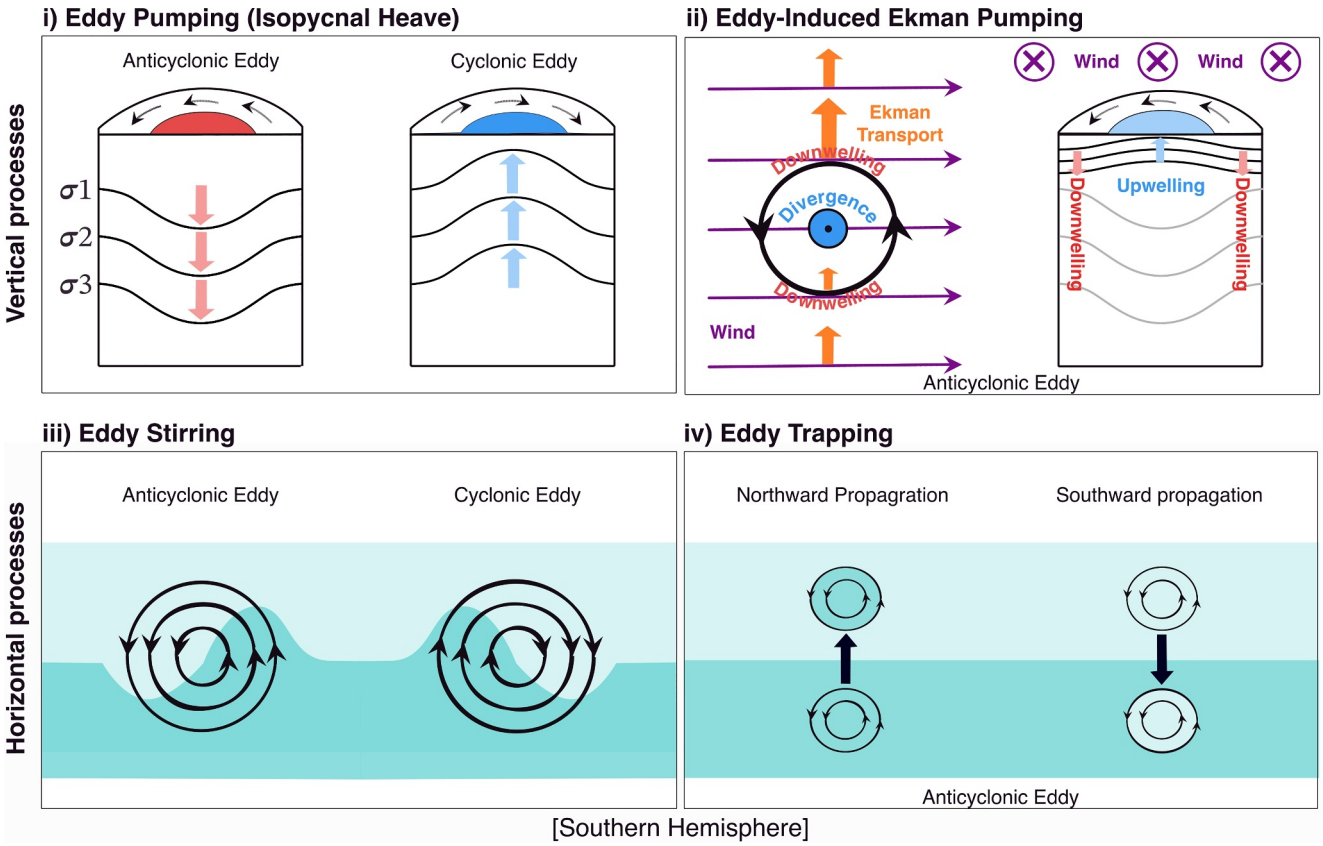

Figure 1. Schematic of the eddy processes for the Southern Hemisphere: (i) eddy pumping (isopycnal heave) for AEs (left) and CEs (right); black arrows indicate the direction of the eddy rotation. Isopycnals ($\sigma1$–$\sigma3$) are illustrated as black curves, where colored arrows indicate the direction of isopycnal heave, with the associated warm (AEs, red, downward) or cold (CEs, blue, upward) cores; (ii) eddy-induced Ekman pumping for AEs from above (left) and the side (right), illustrating the wind (purple arrows and ⊗), Ekman transport (orange arrows, longer arrows mean more transport), and resulting upwelling and downwelling (black lines and colored arrows); isopycnal heave from eddy pumping are illustrated as gray lines for reference; (iii) eddy stirring for AEs (left) and CEs (right); (iv) eddy trapping in AEs with northward (left) and southward propagation (right). Different shades of cyan indicate different water masses and black arrows indicate the direction of the eddy rotation. Note that (ii) illustrates only the relative wind effect, not the vorticity or temperature effects described in Text S2 in Supporting Information S1.

subtropical thermocline (Ito et al., 2010). Studies also show enhanced downward transport of anomalous DIC in higher-resolution models (Swierczek et al., 2021). Suppressed eddy activity in a model of the Drake Passage led to an overestimate of iron supply (Jersild et al., 2021). Model analyses also revealed reduced net phytoplankton population growth rates in CEs concurrent with increased rates in AEs, associated with eddy-induced Ekman pumping (Rohr et al., 2020). These model-based studies highlight processes that merit scrutiny from observations. This is particularly important for assessing future projections of the ocean carbon cycle and marine ecosystems as none of the 19 climate models included in the Intergovernmental Panel of Climate Change (IPCC) Coupled Model Intercomparison Project Phase 6 (CMIP6) included an eddy pump component (Henson et al., 2022).

Eddy detection algorithms applied to satellite altimeter data are an invaluable tool for detecting mesoscale eddies. Argo floats, in turn, sample the oceans much more frequently, in all seasons, and with much greater spatial coverage than ships (Argo, 2000), and combined with altimetric eddy data allow the investigation of the vertical structure of eddies, as previously done for temperature and salinity (e.g., Chaigneau et al., 2009; Frenger et al., 2015; Keppler et al., 2018; Pegliasco et al., 2015), and for oxygen in the North Atlantic (Schütte et al., 2016). Argo floats equipped with BGC sensors have operated in the Southern Ocean for nearly a decade as part of the Southern Ocean Carbon and Climate Observations and Modeling project (SOCCOM; Sarmiento et al., 2023; Talley et al., 2019) and the Global Ocean Biogeochemical Argo array (GO-BGC; Maurer et al., 2021). Combining these tools enables us to better understand the vertical eddy processes affecting the Southern Ocean biogeochemistry and quantify the role of eddies on the carbon cycle.

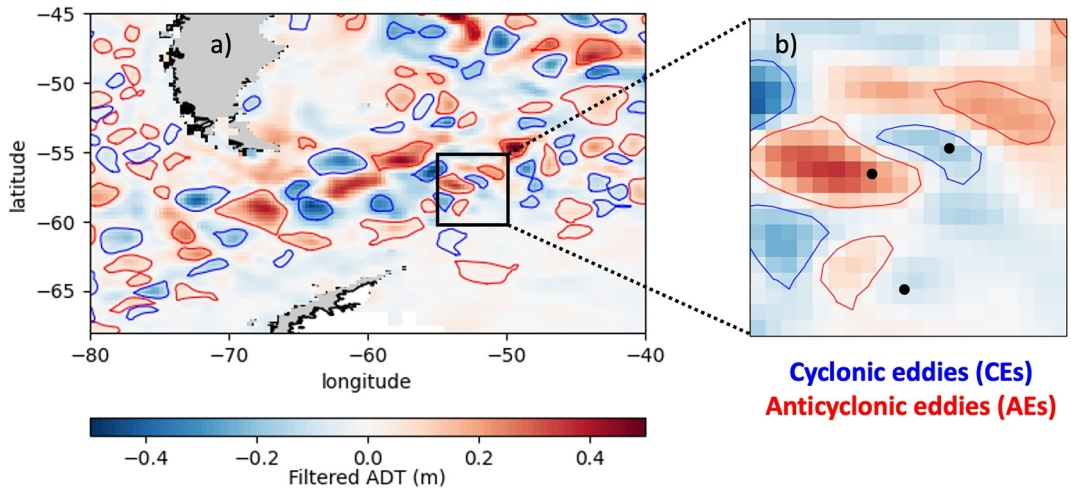

Figure 2. (a) Snapshot of the absolute dynamic topography (ADT) filtered with a high-pass filter (in color) and corresponding detected eddy edges (blue for CEs and red for AEs) on 15 May 2016 near Drake Passage. (b) Enlargement of a subregion with locations of BGC-Argo floats (black dots) to highlight a float inside a CE, inside an AE, and outside of eddies (OE; from north to south).

Frenger et al. (2015) evaluated the physical phenomenology of Southern Ocean eddies, using Core Argo floats, measuring temperature and salinity, co-located with satellite-detected eddies (Argo, 2000). This was followed by a sequence of observation-based BGC studies that were either limited to surface observations (Dawson et al., 2018; Dufois et al., 2014; Frenger et al., 2018), focused on individual eddies or subregions within the Southern Ocean (Dufois et al., 2014; Patel et al., 2020), or focused only on biological parameters (Dawson et al., 2018; Dufois et al., 2014; Frenger et al., 2018; Su et al., 2021). Specifically, Frenger et al. (2018), Dufois et al. (2014), and Dawson et al. (2018) determined the imprint of Southern Ocean eddies on surface chlorophyll-*a* from satellite ocean color; Patel et al. (2020) described the BGC structure of two eddies in the Southern Ocean; and Su et al. (2021) investigated the biological structure of eddies in the Indian sector of the Southern Ocean using float data of chlorophyll and backscatter. With the now 10-year BGC Argo float data set in the Southern Ocean, the surface and subsurface effects of mesoscale eddies on Southern Ocean BGC (DIC, nitrate, oxygen) can be investigated at the full basin scale.

Here, we demonstrate the effects of eddy pumping and eddy-induced Ekman pumping on the vertical distribution of DIC, nitrate, and dissolved oxygen and how these effects vary regionally within the Southern Ocean, in open water north of the sea-ice zone. Further, we disentangle and quantify how much the effects of isopycnal heave and diapycnal or along isopycnal transport each contribute to the overall eddy pumping effects. Last, we quantify the effects of CEs and AEs on the overall Southern Ocean air–sea carbon flux in different subregions and seasons. To evaluate these biogeochemical imprints of mesoscale eddies, from the surface to 1,500 m, we co-locate altimeter-detected eddies with BGC-Argo float measurements from 35°S to the edge of the seasonal sea-ice zone.

2. Data and Methods

2.1. Mesoscale Eddies From Satellite Altimetry

We employ the all-satellite Mesoscale Eddy Trajectory Atlas, version 3.2 (Meta3.2DT; Pegliasco et al., 2022), which uses satellite altimeter data to detect and track eddies in the global ocean. Meta3.2DT is an updated version of eddy detection algorithms by Chelton et al. (2011) and Mason et al. (2014), distributed by the Archiving, Validation, and Interpretation of Oceanographic Satellite data (AVISO). Meta3.2DT includes eddies from January 1993 to February 2022. It detects minima or maxima in the filtered absolute dynamic topography (ADT) as potential eddy centers for CEs or AEs, respectively. The outermost closed ADT contour lines (based on speed) around such extrema are then classified as eddy edges (Figure 2a). We only use Meta3.2DT eddies with a minimum lifetime of 10 days, a minimum radius of 40 km, and a minimum ADT amplitude of 2 cm. The minimum lifetime requirement ensures that the eddies are coherent structures that live long enough to affect BGC significantly. The latter two requirements are due to the reported resolution of the nadir altimeters used by

Table 1
Summary of the Detected Eddies and Co-Located Eddy and Float Profile Properties, After Our Selection Criteria Have Been Applied (for Domain (South of 35°S to the Seasonally Covered Sea-Ice Zone), Period (April 2014–February 2022), Lifetime (> = 10 days), Radius (> = 40 km), and Amplitude (> = 2 cm); See Sections 2.1 and 2.2)

META3.2DT eddy properties in our study	CEs	AEs
Number of detected daily eddy instances	1,618,073 (48.3%)	1,730,769 (51.7%)
Number of detected eddy trajectories	55,186 (50.7%)	53,607 (49.3%)
Mean lifetime ± 2·standard error (days)	80 ± 1	83 ± 1
Standard deviation (days)	129	130
Minimum, median, maximum lifetime (days)	10; 43; 2,460	10; 44; 2,443
Mean amplitude ± 2·standard error (cm)	9.9 ± 0.1	9.1 ± 0.1
Standard deviation (cm)	9.6	8.5
Minimum, median, maximum amplitude (cm)	2.0; 6.4; 117.2	2.0; 6.3; 109.9
Mean radius ± 2·standard error (km)	58.8 ± 0.2	61.1 ± 0.2
Standard deviation (km)	18.1	20.7
Minimum, median, maximum radius (km)	40.0; 53.3; 235.9	40.0; 54.8; 264.8
Mean rotational speed ±2·standard error (cm s^{-1})	22.4 ± 0.1	20.6 ± 0.1
Standard deviation (cm s^{-1})	15.1	12.7
Minimum, median, maximum rotational speed (cm s^{-1})	1.9; 18.0; 155.9	1.5; 16.9; 149.1
Percentage of the area covered (relative to the ice-free Southern Ocean, ~71million km^2)	10.2 ± 0.4%	11.8 ± 0.4%

Co-located profiles and eddies	pH floats	Nitr. floats	Diss. O_2 floats	Temp. floats
Number of profiles in CEs	553 (8.0%)	826 (7.7%)	1,105 (7.8%)	36,750 (8.3%)
Number of profiles in AEs	636 (9.2%)	897 (8.4%)	1,247 (8.8%)	43,233 (9.8%)
Number of profiles OE	5,746 (82.9%)	8,969 (83.9%)	11,851 (83.4%)	360,160 (81.8%)
Total number of profiles	6,935	10,692	14,203	440,143

Meta3.2DT, and they further ensure the coherency of the eddies. See Section 3.1 and Table 1 for a description of the detected eddy properties.

2.2. BGC-Argo and Core Argo Float Data in the Southern Ocean

BGC-Argo floats equipped with pH, dissolved oxygen, nitrate, temperature, and salinity sensors have extensively sampled the upper 2,000 m of the Southern Ocean since 2014 as part of the SOCCOM and GO-BGC projects. We use profiles from SOCCOM's December 2023 data snapshot (see Data Availability Statement). In addition to the measured parameters, which are available through all Argo data centers, the SOCCOM data file includes the derived DIC and pCO_2, as follows. Total alkalinity (TA) is estimated from the observed temperature, salinity, and oxygen, using the Locally Interpolated Estimation of Alkalinity algorithm (LIARv2; Carter et al., 2018). DIC and pCO_2 are then calculated from TA and the observed pH using CO_2 System Calculations (CO2SYS, Sharp, Pierrot, et al., 2023); for pCO_2, a bias correction is first added to pH, following Williams et al. (2017).

We interpolate the float data onto 53 depth levels, which are more closely spaced near the surface than at depth. These are the same depth levels used in the upper 1,500 m of the mapped Argo-based temperature and salinity fields by Roemmich and Gilson (2009). At the time of writing, Meta3.2DT data and the BGC-Argo floats in the Southern Ocean overlap from April 2014 to February 2022. Thus, we only consider floats and eddies from this period and retain only float data with "good" quality flags. For the period overlapping with the Meta3.2DT eddies in the Southern Ocean, 224 active BGC floats collected profiles every 10 days. See Section 3.1 and Table 1 for a description of the statistics of the eddies co-located with BGC-Argo floats.

In addition to the co-measured temperature and salinity on BGC-Argo floats, we use temperature and salinity profiles from the Core Argo array to validate the robustness of our results, which are based on fewer floats from a shorter sampling period. We use all Core Argo profiles in the Southern Ocean from December 2001 to February

2022 with "good" temperature flags (Figure S1 in Supporting Information S1). We interpolate the float data onto the same 53 depth levels as above.

2.3. Co-Locating Eddies and Floats

We co-locate the Meta3.2DT-detected eddies with the floats to identify measurements collected within CEs, AEs, and outside eddies (OE; Figure 2b). When the surfacing location of a float is within the contour line of an eddy, the profile is classified as either CE or AE. If the float surfaces outside of the contour line, it is classified as OE. For more information on the co-location method, see Chaigneau et al. (2011), Pegliasco et al. (2015), and Frenger et al. (2015). Note, however, that those studies relied on the eddy center and the mean radius, assuming circular eddy contour lines, whereas our method makes use of the latest META3.2DT version which includes the eddy contour lines, facilitating more precise co-location than in those earlier studies.

2.4. Vertical Two-Dimensional (2D) Composite Anomalies

We use existing monthly climatologies of DIC, nitrate, dissolved oxygen, temperature, and air–sea CO_2 fluxes as reference data for the anomalies (Text S3 in Supporting Information S1). The 2D composite eddy structures reflect the anomalies as a function of distance to the eddy center (x-axis) and depth (y-axis). We first calculate the anomalies of each DIC, nitrate, dissolved oxygen, and temperature profile within CEs, AEs, and OEs, as follows. As the reference and float data have different sets of uneven depth levels, we first linearly interpolate the reference climatologies onto the same 53 depth levels as the float data. The anomalies are obtained at each depth level by subtracting from the float measurement the climatological value of the month of the float measurement at its 1° grid cell (i.e., the reference data described in Text S3 in Supporting Information S1). For example, for a float measurement on 2 July 2016, we subtract the climatological July value of the reference data set. We do this separately for CEs, AEs, and OEs.

After calculating the anomalies of each profile, we normalize the distance of the profile from the eddy center by dividing it by the radius of that eddy, following Frenger et al. (2015). Here, we use the mean radius of the eddy based on the maximum rotational speed. This provides the distance of an observation relative to the eddy center, where 0 corresponds to the eddy center and 1 to the eddy edge. Note that as our eddy edges can be elliptical, some floats can be within the contour line of the eddy but further away than the mean radius. Hence, the normalized distance can be larger than one, where we set the maximum to 1.3. Assuming that the eddies are azimuthally isotropic, that is, that the anomalies are the same in each direction, we then reflect the data relative to the y-axis to obtain an eddy cross-section, plotted along the x-axis from −1.3 to 1.3.

To compute the 2D composite anomalies at each depth level for CEs and AEs, we interpolate to determine anomalies as a function of normalized distance to the eddy center and depth. For this, we use normalized distances between −1.3 and 1.3, evenly spaced at intervals of 0.1. We then smooth the result horizontally by taking a running mean with a window size of three grid cells (i.e., 0.3R). We conduct this analysis averaged over the whole ice-free Southern Ocean south of 35°S because more data would be necessary for significant results in subregions.

We conduct the same analysis for potential density (σ_θ) to plot the mean isopycnals in the CE and AE composite structures. We first calculate σ_θ based on the co-measured float measurements of temperature and salinity using the Python "seawater" package. Next, we compute the density anomalies as for the biogeochemical and temperature anomalies, using the same float profiles, and plot them as contour lines over the 2D composite anomalies.

Our method of subtracting the monthly 1° climatological values from the observations assumes that this removes any non-eddy signals and isolates the eddy effects. In reality, other modes of variability, including the diurnal cycle and interannual variability, are also present. However, we assume that such signals average out when we take the mean of many profiles inside CEs, AEs, and OEs separately. Similarly, there may be trends in the different reference data sets due to the anthropogenic perturbation, especially in DIC and dissolved oxygen (Gruber, 2011). As more float profiles are available toward the latter part of our period, this could bias the results toward high DIC and low oxygen. However, we conducted an analysis in which we subtracted the linear trend from the profiles before subtracting the reference data to create the anomalies, and the results did not change significantly. We deduce that changing climate is negligible over our relatively short period of less than a decade but may be relevant in future studies that include longer periods.

2.5. Vertical One-Dimensional (1D) Composite Anomalies

We investigate 1D-anomalies of DIC, nitrate, and dissolved oxygen in eddies in multiple subregions as a function of: (i) depth levels, (ii) isopycnals, and (iii) the difference between the two. (i) Depth level anomalies show the overall eddy effects on the vertical distributions. (ii) Isopycnal anomalies reveal any effects not directly caused by isopycnal heaving due to eddy pumping, for instance diapycnal transport, local BGC transformations, or trapped transport of waters from another region. This could also include indirect effects such as an increase in biological and hence oxygen production that might result from nutrients upwelled through eddy pumping. (iii) Subtracting the anomalies on isopycnals from the anomalies on depth levels, after reprojecting the isopycnals to depth space, we isolate the effect of isopycnal heave, that is, water masses moving upward or downward adiabatically (Bindoff & Mcdougall, 1994). For example, upward pumping in CEs leads to isopycnal doming, and hence DIC and nitrate stored at depth are shifted upward. This can make it available to different processes affecting the altered depth, for instance when shifted into the euphotic zone and near-surface mixing layer.

To calculate the 1D-anomalies on depth levels (i, Figure 5 top row), we interpolate every profile and the reference climatology to the same depth levels. We subtract the climatology from every profile to obtain the each profile's anomalies as a function of depth, and then average the anomalies as a function of depth. To calculate the anomalies on isopycnal levels (ii, Figure 5 middle row), we interpolate every profile and the reference climatology to isopycnal levels using σ_θ from the co-measured float measurements of temperature and salinity. We then subtract the isopycnal climatology from every profile's property, to obtain the isopycnal anomalies for every profile as a function of density, and then average the anomalies as a function of density. We then project these average isopycnal anomalies back to the depth of the climatological isopycnals. To calculate the residual anomalies on depth levels (iii, Figure 5 bottom row), which represents heave to the lowest order, we use the profiles from the last step of (ii, i.e., isopycnal anomalies projected to the depth of the climatological isopycnals) and subtract this depth-profile of isopycnal anomalies from the total anomalies on depth levels (i). We conduct this analysis for DIC, nitrate, and dissolved oxygen, each separately for the two subregions defined in Section 2.7.

2.6. Air–Sea CO_2 Flux Anomalies

To estimate the air–sea CO_2 fluxes from the float pCO_2 measurements, we use the parameters provided in the self-organizing maps, feed-forward network (SOM–FFN) estimate that we use as reference data (an update of Bushinsky et al. (2019), see Text S3 in Supporting Information S1). These parameters include the kinetic gas transfer coefficient (k_w in m yr^{-1}), solubility of CO_2 (S_{CO2} in mol m^{-3} μatm^{-1}), sea-ice fraction (f_{ice} in %), and the atmospheric pCO_2 at the marine surface layer (pCO_{2atm} in μatm). See Appendix A3 in Landschützer et al. (2013) for a detailed description of these parameters. We estimate the air–sea CO_2 flux density, F_{CO2}, from the floats in mol C m^{-2} yr^{-1} at each float using SOCCOM's derived surface ocean pCO_2 (pCO_{2ocn} in μatm), estimated from the float-measured pH, temperature, salinity, and oxygen (Section 2.2), in addition to the mapped parameters provided in SOM–FFN at the monthly time-step and 1° grid cell of that float observation, as follows:

$$F_{CO2} = -k_w \cdot S_{CO2} \cdot \left(1 - f_{ice}\right) \cdot \left(pCO_{2atm} - pCO_{2ocn}\right), \quad (1)$$

where positive F_{CO2} is oceanic outgassing and negative is uptake. As we only consider the ice-free Southern Ocean, the sea-ice fraction term is negligible here. We note that the SOM–FFN parameters to calculate the air–sea CO_2 fluxes at the floats are on a coarse-resolution grid (monthly, 1° horizontal). This may add some uncertainty because wind (and thus gas transfer velocity) and sea surface temperature (and thus solubility of CO_2) are highly variable at the subgrid-scale. However, we chose these coarse-resolution values to isolate the eddy effects better. That is, if we were to use point values for these parameters, we would obtain a more accurate flux estimate at the floats, but when comparing these to the coarse-resolution SOM–FFN flux estimates, we would introduce an error: The differences between the float-based flux estimates and the SOM–FFN reconstruction would be partially due to the difference in these chosen parameters and not differences in the pCO_2. With our method of using the SOM–FFN-provided parameters at the coarse resolution, any difference between the float-estimated fluxes and the fluxes in SOM–FFN are due to differences in pCO_2, not differences in calculating the fluxes. See Text S4 in Supporting Information S1 for more details on the flux calculations.

2.7. Domain, Subregions, and Vertical Extent

We define 35°S as the northern boundary of the Southern Ocean and use the seasonally covered sea-ice zone defined by Gray et al. (2018) as our southern boundary (see Figure 2) because the altimetric eddy product does not extend into sea ice. For consistency, we use this southern boundary for all months, that is, regions that are ice-free in Austral summer but have ice cover in Austral winter are excluded. As the reference data for DIC extend only to 1,500 m (Text S3 in Supporting Information S1), we limit the anomalies for all variables to the upper 1,500 m.

We divide the ice-free Southern Ocean into regions with common BGC and physical properties. Southern Ocean regions are often defined using physical data to distinguish frontal zones (Kim & Orsi, 2014; Orsi et al., 1995), but these do not include BGC information. The widely cited global biomes by Fay and McKinley (2014) include chlorophyll-*a* concentrations, but the biomes are also skewed toward physical inputs. Some methods to reconstruct mapped, gap-filled carbon estimates from sparse ship or float observations (e.g., Gregor & Gruber, 2021; Keppler et al., 2020; Landschützer et al., 2016; Rosso et al., 2020) use self-organizing maps or K-means clustering with physical and BGC input parameters. We use K-means clustering weighted toward DIC variations to define our subregions (see Text S5 in Supporting Information S1). The resulting regions are (a) in the ACC and (b) north of the ACC (Figure 3). Our two clusters differ from the five frontal zones by Orsi et al. (1995) in that our clusters subsume their Polar and Subantarctic Fronts into a single boundary that is more zonally uniform than either of those Orsi et al. (1995) fronts. Our ACC boundary is similar to the boundary between the Southern Ocean Subpolar and Subtropical seasonally stratified biomes in Fay and McKinley (2014). In contrast to both of those previous analyses, we exclude the sea ice zone and extend the northern region to 35°S, hence encompassing a Subtropical Front and transition to permanent subtropical stratification.

3. Results

3.1. Properties of the Detected and Co-Located Eddies

From 2014 to 2022, the satellite product identifies daily instances of ~1,600,000 CEs and ~1,700,000 AEs in the Southern Ocean (48% and 52%, respectively, see Table 1), after screening for minimum size and lifetime. These eddy instances are part of ~55,000 CE trajectories and ~54,000 AE trajectories (51% and 49%, respectively). That there are fewer CE instances but more CE trajectories highlights that the CEs in our study are, on average, shorter-lived than the AEs. CEs also have a slightly larger average amplitude, a smaller average radius, and, thus, a larger average rotational speed, in line with the findings by Frenger et al. (2015). See Section 4.3 for a more detailed comparison with that study.

A small subset of satellite-detected eddies had lifetimes longer than 2 years. The longest-lived had a lifetime of 2,460 days, that is, nearly 7 years and many of these are associated with the Agulhas Retroflection. In the temporal definition, some of these extremely long-lived eddies might not technically qualify as mesoscale (i.e., typical lifetimes of months). However, as the maximum radius is on the order of 250 km, we retain these features because they behave like mesoscale eddies in terms of processes. See Text S6 and Figure S4 in Supporting Information S1 regarding these very long-lived eddies. Several had stationary positions and hence are likely to be Taylor columns (Meredith et al., 2015; Prend et al., 2019) or stationary ACC meanders.

We next consider the BGC float profiles co-located with satellite-detected eddies. Our data set has considerably more BGC float profiles with oxygen and nitrate measurements than the pH measurements from which we derive the DIC profiles (Table 1 and Figure 3). Approximately 8% of oxygen and nitrate profiles surface into CEs and AEs, while approximately 8% of pH profiles surface into CEs and 9% into AEs. The remaining ~83% of float profiles surface outside eddies. These statistics are comparable for the more numerous temperature profiles (~8% and 10% in CEs and AEs, respectively). However, based on the eddy area associated with the effective radius, provided in the Meta3.2DT satellite product, the study area is approximately 10% CEs and 12% AEs at any given time, leaving 78% of the area OEs. Thus, we observe a relative undersampling of eddies by the floats, which we discuss further in Section 4.2.

The profiles are distributed rather evenly in the zonal dimension, except for some gaps in the mid-latitude Atlantic and Pacific (Figure 3). There are also considerable meridional gaps, with more profiles in the ACC and fewer profiles toward the north, especially in the eastern South Pacific north of the ACC and southeast and southwest of Australia. These gaps exist for profiles both inside and outside eddies, demonstrating that those regions are less sampled rather than being areas of weak eddy activity. Additionally, there are fewer profiles south of the ACC,

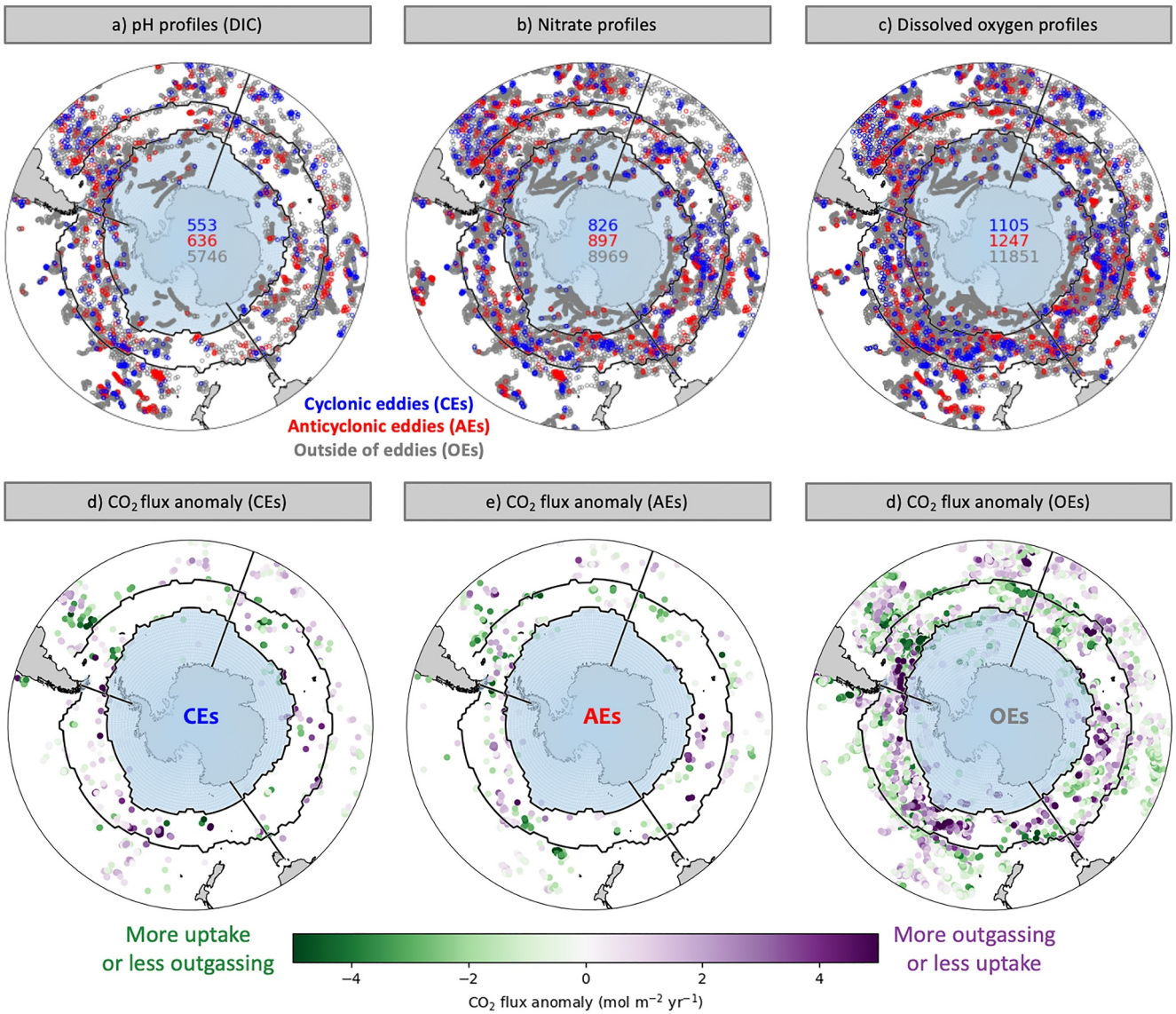

Figure 3. Locations of BGC Argo floats with (a) pH, (b) nitrate, and (c) dissolved oxygen sensors that surface into CEs (blue), AEs (red), and outside of eddies (OEs, gray) between April 2014 and February 2022. Air–sea CO_2 flux anomalies from floats in (d) CEs, (e) AEs, and (f) OEs. Anomalies are relative to mapped fluxes from SOM–FFN (an update of Bushinsky et al., 2019, see Section 2.6). Light blue shading marks the seasonally covered sea-ice zone. The center numbers in (a–c) indicate the number of co-located profiles for CEs, AEs, and OEs only in the ice-free regions. Solid black lines mark the boundaries of the Atlantic, Pacific, and Indian sectors and between the two subregions (in the ACC and north of the ACC). See Figure S1 in Supporting Information S1 for the locations of Core Argo float profiles.

and the profiles in this region are mostly identified as OEs. This is partially because the Meta3.2DT altimeter-based eddy detection does not work over sea ice. This is why we remove the seasonally ice-covered regions in our study, as mentioned in Section 2.7.

The lower panels in Figure 3 show graphically the small number of pH float profiles in eddies versus those outside of eddies. The anomalous air–sea CO_2 fluxes in CEs, AEs, and OEs shown in these panels are discussed and quantified in Section 3.4, where the fluxes are also separated by season. There are many anomalies outside of eddies that are larger than the anomalies inside eddies, suggesting that modes of variability other than eddies may also strongly affect the difference between the point measurements by the floats and the smoother, mapped SOM–FFN product, which we use as reference data for the anomalies. Recent studies of the impact of storms on air–sea CO_2 fluxes, including this BGC float data set, indicate a potential mechanism (Carranza et al., 2024; Nicholson et al., 2022). Further, ACC standing meanders may impact large-scale BGC distributions and air–sea fluxes (Langlais et al., 2017; Vilela-Silva et al., 2024). Although these studies are based on models rather than

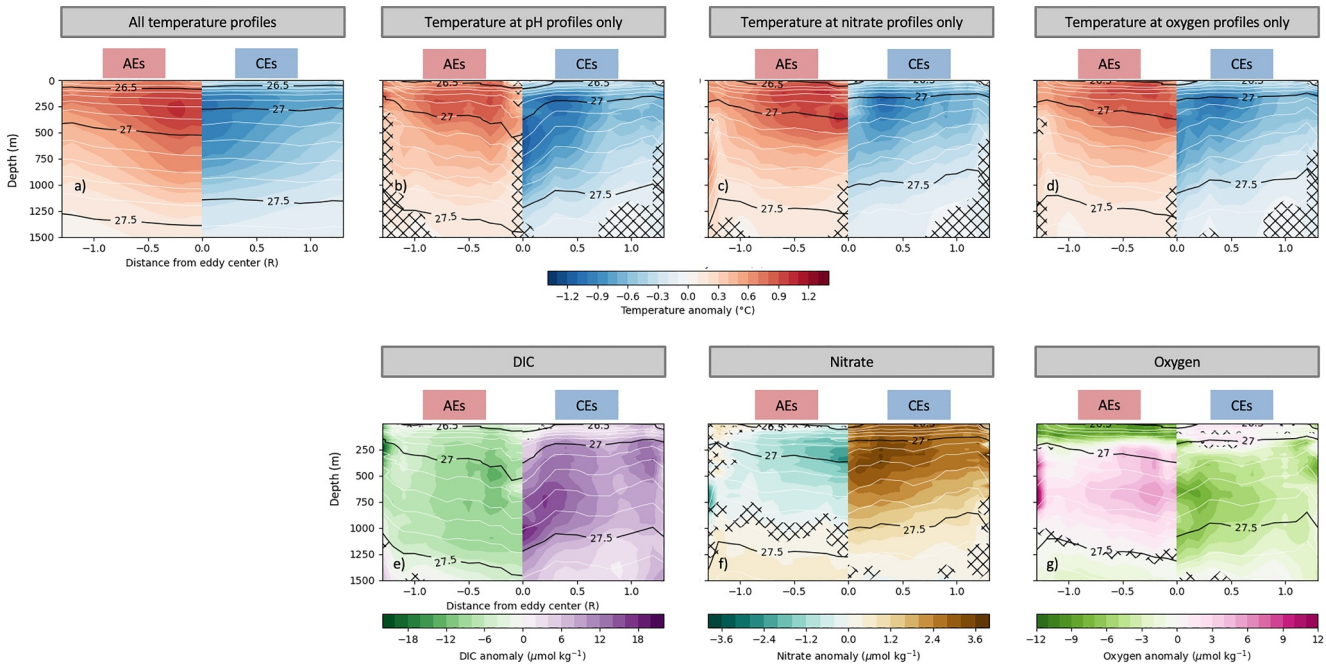

Figure 4. 2D vertical composite structures for the entire sea ice-free Southern Ocean south of 35°S. The top row illustrates the composite temperature anomalies for (a) all Core Argo profiles and for BGC Argo profiles with only (b) pH, (c) nitrate, and (d) dissolved oxygen as a function of the normalized distance from the eddy center (*x*-axis) and depth (*y*-axis) for AEs (left) and CEs (right). The bottom row illustrates the composite anomalies for (e) DIC, (f) nitrate, and (g) dissolved oxygen. Black contour lines mark the potential density (referenced to the surface minus 1,000 kg m^{-3}) at 0.5 kg m^{-3} intervals; white contour lines mark the potential density at 0.1 kg m^{-3} intervals. Hatch marks indicate where the standard error of the mean is larger than the absolute values of the anomalies. Because we calculate the isopycnal anomalies for each variable based on the co-measured temperature and salinity data, the isopycnal anomalies differ slightly in the various subplots, as they are based on different data.

observations, they suggest that standing meanders may be impactful on BGC distributions. We discuss potential sources of representation error associated with comparing point measurements by the floats to the coarse-resolution SOM–FFN data in more detail in Section 4.2.

3.2. Imprints of Eddies on the Subsurface BGC Distributions (2D Vertical Composite Anomalies)

Next, we analyze the mean 2D vertical composite eddy structures averaged over the ice-free Southern Ocean (Figure 4). As a large number of profiles is required to obtain robust composites, we consider the entire study region over all seasons. Before analyzing the BGC composite structures, we test their robustness through a temperature subsampling calculation, as there are many more Core Argo float profiles than BGC-Argo profiles (Figures 3 and 4a–4d, and Figure S1 in Supporting Information S1). We compare the mean vertical structure for temperature using all temperature profiles from the Core Argo array (Figure 4a), which includes ~80,000 profiles inside eddies between 2001 and 2022 (Table 1 and Figure S1 in Supporting Information S1), to the mean vertical structure for temperature using only temperature profiles from the BGC-Argo array, with pH (Figure 4b; ~1,200 profiles), nitrate (Figure 4c; ~1,700 profiles), and dissolved oxygen sensors (Figure 4d; ~2,400 profiles). We find qualitatively comparable vertical composite temperature structures across these Argo float data subsets, with warm anomalies and deeper isopycnals in the water column in AEs and cold anomalies and isopycnal shoaling in the water column in CEs. The signal is stronger between 100 and 500 m and weaker near the surface. Although the standard error is larger than the anomalies in the deeper ocean, the anomalies are significant in most of the upper ocean. Nonetheless, some quantitative differences exist: The temperature composite structure based on only floats with pH sensors (Figure 4b) has slightly larger anomalies than the structures using all temperature floats, whereas the anomalies are slightly smaller when using only floats with nitrate or dissolved oxygen sensors. We attribute this to the fact that we have fewer pH floats, yielding less consistent structures. Overall, the temperature sub-sampling analysis demonstrates that the BGC Argo float array captures relatively well the eddy-driven changes in upper-ocean thermal and density structure as observed by the Core Argo array.

Figures 4e–4g illustrates the vertical 2D biogeochemical imprints of eddies in the Southern Ocean. The DIC and nitrate anomalies (Figures 4e and 4f) are mostly negative for AEs and positive for CEs throughout the water column. The DIC signal is strongest (~15 μmol kg^{-1}) at mid-depth between ~500 and 1,000 m and is still noticeable at 1,500 m. In nitrate, the anomalies are largest (~3 μmol kg^{-1}) between ~200 and 500 m, while the signal is minimal below ~1,000 m. At the surface, the signal in both DIC and nitrate is weakened or even reversed. For dissolved oxygen (Figure 4g), there is a sign switch in the composite anomalies: in the upper ~200 m, the anomalies are negative in AEs and positive in CEs, while below ~200 m, the anomalies are positive in AEs, and negative in CEs. The largest oxygen anomalies are between ~500 and 750 m depth (~10 μmol kg^{-1}).

Because DIC and nitrate concentrations tend to be higher at depth (Sarmiento & Gruber, 2006), these anomalies suggest that the dominant process in the water column is eddy pumping (isopycnal heave, Figure 1a), whereby the downward pumping of water in AEs leads to reduced concentrations of nitrate and DIC while the upward pumping in CEs increases their concentrations (Figures 4e and 4f). For dissolved oxygen, several processes might explain the vertical structures induced by eddies (Figure 4g). To better understand these processes, in Section 3.3 we disentangle the direct effects from isopycnal heaving and indirect effects such as changes in biological production and diapycnal and along-isopycnal transport on these anomalies. In DIC and dissolved oxygen, air–sea gas exchange may further weaken the surface signal or amplify it due to the temperature sensitivity of carbon and oxygen solubility in seawater.

The effect of eddy pumping emerges clearly in the isopycnal displacements (Figure 4): isopycnals in the interior water column are deepened in AEs and uplifted in CEs. However, near the surface, the isopycnals in AEs and CEs align, suggesting that eddy-induced, wind-driven Ekman transport may offset the effects of eddy pumping. Another intriguing feature of the isopycnal anomalies is that while they are deepened in AEs and heaved upward in CEs, they are not as dome-shaped as might have been expected. Instead, the isopycnal anomalies are relatively flat across the eddy diameter. The relatively flat isopycnals could be due to stratification. We suspect different sources of variability affect the isopycnals, and the resulting low signal-to-noise ratio leads to these rather flat isopycnal anomalies. The flat anomalies could be due to the nature of solid body rotation, or due to winds that may cap some of the variability, especially given the deep mixed layers in the Southern Ocean. Further, our smoothing using a running mean (Section 2.4) could contribute to this flattening too. Overall, we conclude that of the two eddy processes that affect the vertical distribution, eddy pumping dominates through most of the water column. Eddy-induced Ekman pumping only partially offsets this effect, although it may dominate near the surface.

3.3. Regional Analysis of Different Processes (1D Vertical Composite Anomalies)

We further delve into the processes driving these eddy-induced anomalies in the vertical structure of DIC, nitrate, and oxygen (Figure 5). We now divide the Southern Ocean into two regions with differing background vertical gradients: the upwelling region in the ACC and the subduction region north of the ACC. To increase the number of profiles in the two regional averages, we have not separated the Atlantic, Pacific, and Indian sectors. In Figure S2 in Supporting Information S1, we show that the anomalies are similar in the three sectors.

The mean vertical 1D anomalies on depth levels (Figure 5, top row) include direct effects of adiabatic isopycnal heave and indirect effects, including eddy-induced changes in biological production and diapycnal and along-isopycnal transport. As highlighted in Section 3.2 and the 2D composite analysis, negative DIC and nitrate anomalies occur in AEs, while positive DIC and nitrate anomalies occur in CEs (Figures 5a, 5b, 5g, and 5h). In dissolved oxygen (Figures 5m and 5n), negative anomalies occur in the upper ocean (0–250 m) in AEs with positive anomalies at depth; the pattern is the opposite in CEs. The sign shift occurs around ~200 m in the ACC and ~500 m north of the ACC, consistent with winter mixed-layer depths in the two regions. The nitrate profiles in the ACC slant with depth, with more positive anomalies toward the surface. However, if the eddy effects are truly isolated with this method, the profiles OEs should be centered around zero. We anticipated that this slant may be due to differences between the reference climatology from the World Ocean Atlas 2018 (WOA18; Boyer et al., 2018) and the float data period, because WOA18 is primarily based on data from decades prior to most of the floats (1955–2017; see Text S3 in Supporting Information S1). Another interesting feature in the nitrate anomalies in the ACC is that the profiles in CEs, AEs, and OEs converge around 800 m. We attribute this to the minimal vertical gradient in nitrate in the mean background signal at those depths (Figure S3 in Supporting Information S1); thus, upward or downward pumping would not have a noticeable impact on the distribution at this depth.

10.1029/2024AV001355

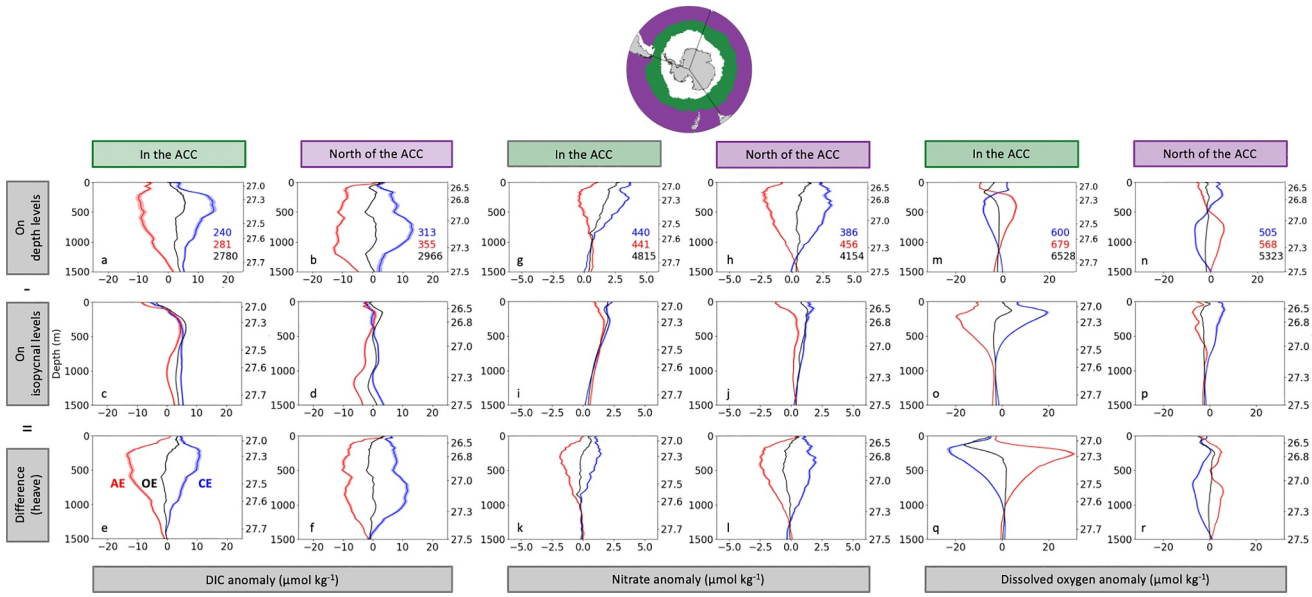

Figure 5. Mean vertical 1D composite anomalies in two subregions of the Southern Ocean: in the ACC (green) and north of the ACC (purple). Mean vertical anomaly profiles (thick lines) of DIC (a–f), nitrate (g–l), and dissolved oxygen (m–r) for AEs (red), CEs (blue), and OEs (black); shading illustrates the standard error about the mean. Anomalies are computed on depth levels in meters (top row), on isopycnal levels reprojected to depth (middle row), and are differenced, that is, top row minus middle row (bottom row), representing the heave. In all three rows, the left *y*-axis illustrates the depth, and the right *y*-axis illustrates the corresponding isopycnal. The numbers in color in the top row indicate how many profiles were used to create the averages for CEs (blue), AEs (red), and OEs (black). OE profiles tend to be centered around zero, as expected by definition.

Property anomalies on isopycnals (Figure 5, middle row) contribute to the total anomalies (top row). Isopycnic changes are due to a range of processes such as transport across and along isopycnals or biogeochemical feedbacks arising from changes in nutrient supply, biological production, and consumption, that is, processes that are only indirectly related to isopycnal heave. Isopycnic anomalies also reflect trapping and transport of water properties laterally (Figure 1iv). In DIC and nitrate, there is very little along-isopycnal change in both subregions (Figures 5c, 5d, 5i, and 5j) compared with the total signal (Figures 5a, 5b, 5g, and 5h). One might have expected a signal in DIC if enhanced nutrients in CEs were enhancing biological consumption of inorganic carbon, leading to negative DIC anomalies, as proposed by Harrison et al. (2018). That study found that export rates differ at regional scales when eddies are resolved in a global Earth system model. We do not observe this effect in our data, likely due to the lag between enhanced nutrient supply and the decrease in DIC that is obscured by the averaging of profiles across all periods of eddy lifetime. There may also be a seasonal influence that is averaged out in our year-round analysis.

In contrast, for dissolved oxygen, we find a large signal on isopycnals (Figures 5o and 5p): negative oxygen anomalies in AEs, and positive anomalies in CEs (up to ~12 μmol kg^{-1} in the ACC and ~5 μmol kg^{-1} north of the ACC). The largest anomalies on isopycnals occur in the upper ocean above 800 m. If nutrient availability were the principal control (e.g., upwelled nutrients in CEs leading to enhanced biology), we would see opposing signals close to the surface, where photosynthesis is dominant, compared to at depth, where respiration dominates. Hence, we hypothesize that eddy trapping (Figure 1iv) plays a major role. If AEs tend to propagate from low to high oxygen regions (and CEs from high to low), this could explain the observed anomalous oxygen signals on isopycnals. This is supported by positive temperature anomalies on isopycnals for AEs and negative for CEs observed in our analysis (not shown).

Taking the difference between the anomalies on depth levels (Figure 5, top row) and isopycnals (Figure 5, middle row) isolates the direct changes of the properties due to isopycnal heaving (Figure 5, bottom row), that is, the downward or upward movement of the isopycnals due to eddy pumping and eddy-induced Ekman pumping. In DIC and nitrate, the direct effects from the heave (Figures 5e, 5f, 5k, and 5l) are very similar to the overall anomalies on depth levels (Figures 5a, 5b, 5g, and 5h) because the anomalies on isopycnals are so small (Figures 5c, 5d, 5i, and 5j). Here, we find negative anomalies in AEs, associated with the downward movement of

the isopycnals, and positive anomalies in CEs, associated with the upward movement of the isopycnals. Thus, we conclude that the overall imprints of eddies on DIC and nitrate are primarily due to the direct effects of isopycnal heaving. However, for dissolved oxygen, the isopycnal heave effect (Figures 5q and 5r) differs substantially from the net effect (Figures 5m and 5n): here, isopycnal heave drives positive anomalies in AEs, which we attribute to the oxygen-rich surface waters moving downward, and negative anomalies in CEs, which we attribute to the oxygen-depleted deep water moving upward (up to $\sim 25 \mu$mol kg^{-1} in the ACC and $\sim 8 \mu$mol kg^{-1} north of the ACC). Because the diapycnal oxygen anomalies (Figure 5, middle row) oppose the anomalies associated with the isopycnal heave (Figure 5, bottom row), the net effect (Figure 5, top row) is considerably smaller than the individual effects. Additionally, because the two individual effects have their maxima at different depths, the net effect switches sign around 200 m.

The anomaly profiles also reveal regional differences: the largest anomalies in all three variables are deeper north of the ACC (~500–700 m) than in the ACC (~200 m). The pycnocline and hence penetration of high vertical property gradients are deeper in the subduction region north of the ACC than in the upwelling region in the ACC (see Figure S3 in Supporting Information S1). Further, DIC and nitrate anomalies are larger north of the ACC than in the ACC because the DIC and nitrate gradients are steeper in the former. Additionally, there are differences between the vertical structures in DIC and nitrate, with the largest nitrate anomalies occurring at shallower depth than the largest DIC anomalies. The anomalies in nitrate are negligible below ~1,000 m in most regions, while the DIC anomalies are still significant at 1,500 m in most regions. We attribute this contrast to differences in the mean background profiles of DIC compared to nitrate profiles, which exhibit a shallower enhanced gradient. Contrary to the DIC and nitrate anomalies, the magnitude of the overall oxygen anomalies on depth levels is similar in the two subregions, possibly because the effects cancel each other out. Both for the isopycnal heave effect and non-heave effects, the oxygen anomalies are larger in the ACC where the oxygen gradients are more pronounced (see Figure S3 in Supporting Information S1).

3.4. Eddy Effects on Air–Sea CO_2 Fluxes

Patterns in air–sea CO_2 fluxes in AEs and CEs over all seasons and regions do not appear to differ much from fluxes in OEs (Figures 3d–3f). A clearer picture emerges when we quantify the mean anomalies and the integrated flux anomalies associated with AE, CE, and OE float profiles (Figure 6). On average, CEs are associated with weak additional outgassing or less uptake (Figures 6a–6d), with a total mean anomalous outgassing by CEs of 0.01 ± 0.01 Pg C yr^{-1} ($\sim -2 \pm 2\%$ of the mean fluxes in the region in SOM–FFN), which is not statistically significant. In contrast, AEs are, on average, associated with additional uptake or less outgassing (Figures 6e–6h), with a total mean anomalous uptake by AEs of 0.03 ± 0.01 Pg C yr^{-1} ($\sim 7 \pm 2\%$ of the mean fluxes in the region in SOM–FFN). These findings align with our results from Sections 3.2 and 3.3, where we found positive DIC anomalies in CEs and negative DIC anomalies in AEs associated with eddy pumping (isopycnal heave), which is only slightly weakened by eddy-induced Ekman pumping near the surface. Additional surface DIC in CEs increases the ocean surface pCO_2, leading to enhanced outgassing or decreased oceanic uptake in CEs, and the opposite for AEs (see Equation 1). Given the nearly equal numbers of CEs and AEs, the net effect is only a small change in the net air–sea flux.

If our method and sampling density could completely isolate eddy effects, the OE air–sea flux anomalies should, by definition, be zero. Indeed, the large anomalies in OEs (Figures 3d–3f) mostly cancel when we average over the regions and seasons, leading to comparably small mean anomalies in OEs (Figures 6i–6l). However, in most regions and seasons, the integrated OE flux anomalies are significantly different from zero, except during summer (-0.02 ± 0.03 Pg C yr^{-1} in the ACC and 0.03 ± 0.03 Pg C yr^{-1} north of the ACC) and during winter in the ACC (0.01 ± 0.03 Pg C yr^{-1}). This suggests that there is a difference between the float measurements and the mapped SOM–FFN reference product in some regions and seasons, even though the SOM–FFN run we use is weighted toward the floats (Section 4.2). This caveat must be considered when interpreting the effects of CEs and AEs. The integrated anomalous signal in OEs in all regions and seasons (-0.01 ± 0.02 Pg C yr^{-1}) is not significantly different from zero, indicating that there is no overall bias, and the different noise sources cancel with enough averaging. When we consider the overall effect of CEs and AEs combined, we add 0.01 Pg C yr^{-1} from the potential OE offset to the uncertainty using standard error propagation, which yields a net eddy effect of $\sim 0.02 \pm 0.02$ Pg C yr^{-1}, equivalent to $\sim 5 \pm 5\%$ of the total carbon uptake. These findings also align with the results by Resplandy et al. (2019), who used a submesoscale-permitting biophysical model to quantify the impact of eddies

10.1029/2024AV001355

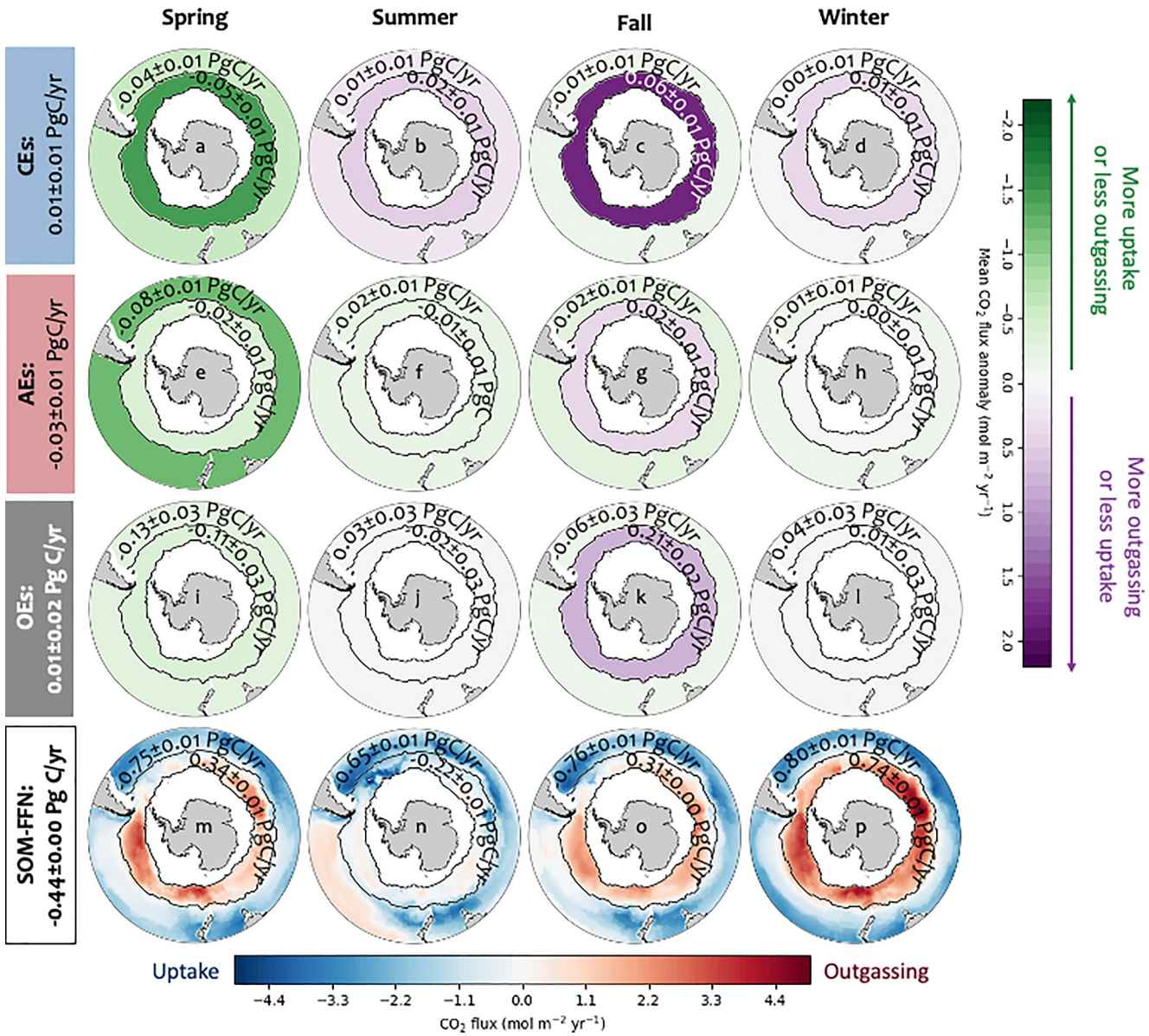

Figure 6. Air–sea CO_2 flux anomalies in the ice-free Southern Ocean in CEs (a–d), AEs (e–h), OEs (i–l), and the mean flux from the SOCCOM-weighted SOM–FFN run (m–p; an update of Bushinsky et al., 2019, see Section 2.6) during austral spring (a, e, i, m), summer (b, f, j, n), fall (c, g, k, o), and winter (d, h, l, p), where spring refers to September, October November; summer to December, January, February; fall to March, April, May, and winter to June, July, August. Anomalies are relative to the mapped SOCCOM-weighted SOM–FFN product at the timestep of the observation. The numbers in each subplot are the integrated fluxes or flux anomalies in Pg C yr^{-1} in each region and season ± the standard error of the observations. Note that the mean flux anomalies (shading in μmol m^{-2} yr^{-1}) can be small while the corresponding integrated flux anomalies (numbers in Pg C yr^{-1}) are large (e.g., in OEs) because the integrated flux anomalies consider the fraction of the area that is covered by eddies (see Section 2.6). The numbers on the left are the total integrated annual flux anomalies in CEs, AEs, OEs (top three rows), and the total integrated annual flux in SOM–FFN (bottom row).

on the biological carbon pump. They found that downward eddy pumping (heave) in AEs can transfer carbon below the mixed layer, but due to the opposing effects of cyclonic and anticyclonic eddies (upward and downward pumping, respectively), the overall effect of eddies on the annual flux was less than 5%.

Beyond these general features in CEs and AEs, some noteworthy seasonal and regional differences exist. The most striking and significant seasonal signals in the eddy air–sea flux anomalies are: (a) outgassing in fall and uptake in spring in CEs in the ACC (Figures 6a and 6c), and (b) uptake in AEs north of the ACC in spring (Figure 6e). These contrast with weak eddy air–sea flux anomalies in summer and winter (Figures 6d and 6h). We

also note that the fluxes in the ACC CEs (Figures 6a–6d) are significantly larger than the ACC AEs (Figures 6e–6h) in all seasons. These also contrast with seasonality of the total air–sea flux in SOM–FNN, which has the strongest outgassing in winter (Figure 6p), in the ACC, and strong uptake throughout the year north of the ACC (Figures 6m–6p).

In the ACC, the anomalous fall outgassing in CEs is 0.06 ± 0.01 Pg C yr^{-1}, which is $19 \pm 3\%$ of the mean flux in that season and region in SOM–FFN (0.31 ± 0.00 Pg C yr^{-1}) (Figure 6o). Even if the mean CE fall anomalies (2.0 μmol m^{-2} yr^{-1}) are offset by the mean signal in OEs (0.8 μmol m^{-2} yr^{-1}, yielding a corrected mean CE signal of 1.2 μmol m^{-2} yr^{-1}), the integrated anomalies stand out as a region of significant anomalous outgassing. We note that there is also an outgassing signal in the fall in the ACC in both AEs (0.02 ± 0.01 Pg C yr^{-1}) and OEs (0.21 ± 0.02 Pg C yr^{-1}) (Note that the total flux for OEs is much larger than for CEs because the total area of OEs is much larger; however, the flux per unit area is much larger in CEs than OEs). We speculate that this strong anomalous outgassing is associated with weakened stratification and deepening of the mixed layer in the fall due to cooling, which entrains the higher underlying DIC regardless of the eddy structure (Talley et al., 2011). A CE, with upward eddy pumping, would enhance the upward penetration of high DIC to the sea surface compared with OEs and downward-pumping AEs. The enhanced surface DIC then increases the surface pCO_2, explaining the enhanced outgassing (Equation 1). This is a fall eddy enhancement of the obduction process that dominates the winter outgassing in the ACC (Prend, Gray, et al., 2022). This mechanism would not be operative in summer (0.02 ± 0.01 Pg C yr^{-1}), when the mixed layer is shallow, or in winter (0.01 ± 0.01 Pg C yr^{-1}), when the already deep mixed layer is not deepening further, leading to a mostly eddy-induced additional isopycnal heave, but not as much additional entrainment of DIC.

In contrast, during spring, both AEs and CEs induce more carbon uptake (or less outgassing) in both subregions. However, in spring, we also observe large negative mean anomalies in OEs (-0.13 ± 0.03 Pg C yr^{-1} north of the ACC and -0.11 ± 0.03 Pg C yr^{-1} in the ACC), indicating that the floats may be biased negatively here compared to the SOM–FFN reference product. Accounting for this potential offset, the anomalies are only significantly positive for CEs in the ACC and for AEs north of the ACC. We hypothesize that for CEs in the ACC in spring (-0.04 ± 0.01 Pg C yr^{-1}), the anomalous uptake is associated with the effects of biological production. CEs pump nutrients upward through isopycnal displacement (Sections 3.2 and 3.3), enhancing biological production, especially in the spring when more light becomes available. We argue that the enhanced biological production then leads to the export of inorganic carbon, that is, a decrease in DIC and thus pCO_2, leading to more oceanic carbon uptake. In spring, the water is still less stratified with deeper mixed layers, allowing for diapycnal export of inorganic carbon. We suspect this signal is not apparent in summer, when light is much more available, because the mixed layer is then shallower than in spring, inhibiting the diapycnal export of inorganic carbon. Conversely, we hypothesize that the anomalous spring uptake in AEs north of the ACC (-0.08 ± 0.01 Pg C yr^{-1}) is associated with enhanced carbon export during this season due to increasing light availability. This process is further enhanced by AEs pumping water downward which facilitates additional oceanic uptake. This signal is weaker in the ACC, likely because the upwelling background circulation dampens the downward eddy pumping signal.

4. Discussion

4.1. Different Drivers for Different Tracers

It may be counter-intuitive that some tracers may be affected more intensely by some physical drivers than others, for example, how can DIC and nitrate anomalies be related to different eddy-induced drivers than oxygen anomalies? Our understanding is that because there are different processes at play, which sometimes counteract and sometimes reinforce each other, the mean background gradient of a tracer can affect which process(es) will dominate. As DIC and nitrate have more similar background gradients in our study region, they tend to be dominated by similar processes, whereas the background gradient of dissolved oxygen is different (see Figure S3 in Supporting Information S1).

This is consistent with the evidence for eddy trapping found by Frenger et al. (2015) using a much larger core Argo data set. These oxygen and temperature anomalies suggest that a different water mass is trapped in these eddies, down to a depth of 800–1,000 m (density of 27.6 σ_θ in the ACC and density of 27.3 σ_θ north of the ACC). Targeted observation-based and modeling process studies should further investigate the effects of eddy trapping on the Southern Ocean BGC, which cannot be disentangled using the float data alone at a basin scale. We also

note that the oxygen anomalies in OEs are at times not centered around zero, which we attribute to differences between the float data and the reference climatology (GOBAI-O2, see Section 4.2).

4.2. Caveats and Sources of Uncertainties

4.2.1. Eddy Definition

Our analysis uses the META3.2DT eddy definition based on closed high-pass filtered ADT contours and subjectively chosen criteria to remove non-eddy structures. A different detection algorithm and selection criteria could alter the eddy statistics. Using the geometric definition of an eddy based on the ADT contour lines may introduce uncertainties in the eddy edge. Moreover, META3.2DT eddy-detection algorithm slightly differs from previous AVISO versions, TOEddies by Laxenaire et al. (2018), and the Multiparameter Eddy Significance Index (MESI; Roman-Stork et al., 2023). Thus, floats in small/weak eddies or close to an eddy edge may or may not be classified as inside an eddy, depending on the product used. However, we anticipate that such discrepancies would average out over the large regions considered here. Similarly, our exclusion of short-lived eddies (lifetimes <10 days) and small eddies (radii <40 km and amplitudes <2 cm), which eliminated spurious features, and the inclusion of very long-lived eddies may add further uncertainty. Taken together they may have a noticeable impact on the biogeochemical profile averages. Follow-up studies could compare the vertical eddy structures using different eddy definitions, leveraging the larger number of core Argo floats.

4.2.2. DIC and pCO_2 Estimates

Part of our analysis relies on DIC and pCO_2, which are derived from the BGC float sensor data. In a thorough comparison of derived float and bottle-sample DIC, Metzl et al. (2024) found that the average values in the upper 100 m were almost identical, and that float profiles below 200 m were also consistent with bottle measurements. This is encouraging for our analysis of water column DIC anomalies. In contrast, there is ongoing discussion about bias in BGC float estimates of pCO_2 (and thus air–sea carbon flux) compared with direct ship measurements (Bushinsky et al., 2019; Gray et al., 2018; Jin et al., 2024) as noted by aircraft atmospheric estimates (Long et al., 2021). However, the Metzl et al. (2024) comparison supports robust estimates from the float data set, which contains considerably more data points than ship data sets, allowing robust analysis within the uncertainties and caveats we describe. Further, we are investigating only the anomalies of the air–sea CO_2 flux, and not the absolute value, which reduces the impact of possible bias. Finally, we use a mapped monthly climatology of the fluxes that is weighted toward float observations as a reference value (see Section 2.6). Thus, potential discrepancies between float and ship pCO_2 data should not significantly affect our flux anomaly analysis.

4.2.3. Representation Error

In our 1D vertical profile analysis (Figure 5), the mean anomalies OEs should be, but are not always centered around zero and sometimes display gradients or high variability in the vertical. Similarly, the seasonal mean air–sea CO_2 flux anomalies in OEs (Figure 6) are also at times significantly different from zero. We attribute this to representation error (sampling error), that is, the float observations are point measurements that may not be representative of the 1° monthly grid cell, especially in light of sub-monthly and sub-grid variability, including the diurnal cycle and storms (Carranza et al., 2024; Nicholson et al., 2022). This representation error could lead to a situation where subtracting the monthly climatology does not completely isolate the eddy signals. Investigating the different modes of variability in the Southern Ocean carbon budget remains an active topic of research and is beyond the scope of this study (Keppler & Landschützer, 2019; Landschützer et al., 2015). Additionally, the monthly climatologies we use as reference data sets may not fully represent the Southern Ocean state during our period. Although our reference fields of Mapped Observation-Based Oceanic DIC (MOBO-DIC; Keppler et al., 2023b) and the Global Gridded Monthly Data set of Ocean Interior Dissolved Oxygen (GOBAI-O2; Sharp, Fassbender, et al., 2023) are based on observations, they are data estimates that fill very large gaps in time and space and thus have large uncertainties. The reference field for nitrate, WOA18, is based on data collected between 1955 and 2017, that is, mostly before the float observations, and its mean field could have changed, for example, due to anthropogenic perturbation of the Earth system.

Similarly, for our analysis of the eddy effects on the air–sea CO_2 fluxes (Section 3.4), the floats are individual point measurements inside eddies, at different distances from the eddy centers. We have assumed that averaging all point measurements within all eddies represents the average anomalies inside eddies, but undersampling

results in uncertainty in the average. Further, the standard error of the mean only includes the variability of the observations in a region and season and does not include measurement uncertainty, for example, associated with the sensor calibrations or the CO_2 flux estimates (Landschützer et al., 2013; Williams et al., 2017).

The relatively small number of float profiles may render it difficult to obtain robust statistics, as any outliers may affect the mean significantly. Reassuringly, as seen in Figures 4 and 5, the standard error is small enough to allow detection of significant differences between AEs, CEs, and OEs. Second, mode water (intra-thermocline) eddies, which are identified as AEs in eddy-detection algorithms based on SLA or ADT but have an eddy-pumping signature similar to CEs (Frenger et al., 2018; Karstensen et al., 2017; McGillicuddy et al., 2003), are part of our data set. We suspect that this may weaken our mean AE anomalies. Third, our temperature testbed analysis (Figures 4a–4d) demonstrates that care should be taken when interpreting fine-scale features in eddy composites of DIC, nitrate, and dissolved oxygen. The BGC anomalies are based on considerably fewer observations than the Core Argo array (less than 3%). We anticipate that with continued BGC-Argo float deployments, a more robust quantitative analysis of the role of eddies in the Southern Ocean carbon, nitrate, and oxygen budgets can be conducted.

4.2.4. Float Sampling Density

As demonstrated in Table 1 and discussed in Section 3.1, we find an intriguing observation: fewer BGC Argo floats surface into eddies (both CEs and AEs) than the expected percentage based on the average eddy coverage. This represents a spatial sampling bias. This may reflect the tendency of Lagrangian floats to accelerate toward strongly eddying currents (Davis, 1991; Freeland et al., 1975), as observed for BGC floats deployed in SOCCOM (Talley et al., 2019) and as modeled recently by Wang et al. (2020). A localized version of this process, that is, the potential inhibition of the penetration of floats into the interior of mesoscale eddies, could be a topic of further investigation, as highlighted by Dove et al. (2021), who found that floats are strongly limited by the fact that they rarely cross regions of strong strain due to their quasi-Lagrangian nature.

4.3. Comparison With Previous Eddy–Float Studies

We first compare our co-located eddy characteristics and temperature structures with Frenger et al. (2015)'s Southern Ocean study. They analyzed ∼13,000 Core Argo temperature profiles located within eddies between 1997 and 2010 (13 years). Our more recent 8-year Core Argo data set has more temperature profiles inside eddies (∼20,000 in CE, ∼24,000 in AEs, hence ∼44,000 total inside eddies). Our larger number might be due to a larger number of floats. But more importantly, Frenger et al. (2015) considered eddies with a lifetime longer than 1 month compared with our choice of 10 days. Counterintuitively, their study found a shorter mean eddy lifetime than ours (70 days), as they find fewer very long-lived eddies, with the longest lifetime being ∼3 years. This is likely due to a difference in the way eddy trajectories were identified. Similar to our study, they also found slightly fewer CEs than AEs (47.1% and 52.9%, respectively), but a slightly larger mean amplitude of 12 cm, likely because they only considered longer-lived eddies. We do not compare radii as they reported only the radius of the eddy core and not the radius relative to the eddy edge. Comparing the 2D vertical temperature composites with Frenger et al. (2015), both studies show the largest temperature anomalies of approximately 1°C between ∼200 and 500 m depth. Their study and ours find that the largest anomalies are not directly at the eddy center but at approximately 1/3 of the eddy radius.

Our findings, that the DIC and nitrate anomalies are larger north of the ACC than in the ACC and that the largest anomalies are deeper north of the ACC than in the ACC, align with Frenger et al. (2015)'s temperature and salinity structures. Our finding of low oxygen and high temperature on isopycnals in AEs, and the opposite in CEs, is consistent with Frenger et al. (2015)'s finding of eddy trapping, based on temperature anomalies. They showed that trapping transports heat, and so we might infer that trapping also transports oxygen. Their findings about eddy stirring, which is an equally effective transport mechanism, could not be tested with our much sparser data set. In a subsequent study, Frenger et al. (2018) found that north of the ACC, CEs had positive surface chlorophyll-*a* anomalies, while in the ACC, the anomalies were negative. The opposite was true for AEs. They attributed these regional differences mostly to lateral advection by eddy stirring and associated entrainment, which can offset or enhance the effects of eddy pumping. However, they also acknowledged that multiple processes could be simultaneously at play.

While Argo floats with oxygen sensors are more numerous than full-sensor BGC Argo floats such as in SOCCOM, there have been relatively few studies of oxygen structure in eddies, and most have focused on tropical oxygen minimum zones. Notably, Schütte et al. (2016) found large eddy-induced reductions of dissolved oxygen associated with the tropical North Atlantic's shallow oxygen minimum zone, using glider and BGC-Argo float data. AEs and CEs both exhibited negative oxygen anomalies between 50 and 150 m, with AE anomalies nearly double CE anomalies (−79 vs. −38 μmol kg^{-1}). The large oxygen reductions imply efficient trapping of water in the eddies and high biological activity (Karstensen et al., 2017). These tropical oxygen reductions are much larger than our mean maximum oxygen anomalies (−8 μmol kg^{-1} and −7 μmol kg^{-1}, at depths of ∼400 m and ∼1,000 m, in the ACC and north of the ACC, respectively; Figure 5). As the magnitude and depth of the anomalies depend on the background gradients, surface stratification, and biological activity, these differences are expected, for example, due to deeper mixed layers in the Southern Ocean than in the tropical North Atlantic. Interestingly, that same study, as well as others (Karstensen et al., 2017; Köhn et al., 2022), primarily focused on the eddies' low-oxygen imprints, whereas we found a reversing signal with an anomaly sign switch at the surface and at depth. Again, this is expected due to the different oxygen background gradients and processes at play in the Southern Ocean. This finding may be relevant for model parameterization, which tends to apply eddy advection and diffusion homogeneously to tracers without considering BGC processes within eddies and tracer-unique transformations. Future comparisons of the observations to modeled and parameterized eddy imprints on BGC may help elucidate how to focus such improved parameterizations. Before developing such parameterizations, an important question concerns quantifying eddy impacts on oxygen ventilation, transport, and cycling that consider these spatial differences.

Both Frenger et al. (2018) and Dawson et al. (2018) reported a seasonal sign switch of eddy-induced chlorophyll anomalies in the ACC associated with eddy modification of the mixed-layer depth. This aligns with our finding of the seasonal sign switch in CE carbon fluxes in the ACC, with strong negative anomalies in spring and strong positive anomalies in fall. Dufois et al. (2014) investigated the surface chlorophyll anomalies in the Indian sector of the Southern Ocean and found AEs to have higher chlorophyll concentrations than CEs, which is the opposite of what would be expected from eddy pumping. They argued that adjustments of the seasonal mixed layer in eddies may be causing these anomalies. Liu et al. (2023) found that about 1/4 of the eddies in the Southern Ocean showcase an "abnormal" signature: cold SSTs with increased surface chlorophyll-*a* in AEs and warm SSTs with decreased surface chlorophyll-*a* in CEs. They attribute this "abnormality" largely to Ekman pumping. Su et al. (2021) investigated the subsurface chlorophyll-*a* anomalies in the offshore Indian sector of the Southern Ocean. They found that chlorophyll-*a* anomalies in the upper 200 m were positive both in AEs and CEs, which they attributed to eddy-induced Ekman pumping and deep vertical mixing in AEs and eddy pumping in CEs. This is inconsistent with our findings that AEs and CEs tend to have opposite signals. However, Su et al. (2021) separated the signal by season and subdivided the Indian sector into subregions. Some of those subregions and seasons have opposite signals for AEs and CEs, which are large regions with many floats. Because we average the profile anomalies over large regions, our analysis can only inform us about these averages, while we are aware that individual eddies may have very different, and even opposing BGC signatures.

4.4. Other Mechanisms

Beyond the two vertical processes emphasized here, the horizontal processes of stirring and trapping (Figure 1) could also affect Southern Ocean BGC. We have shown evidence for eddy trapping based on oxygen anomalies on isopycnals in CEs and AEs, but do not have a sufficient data set to study stirring (see Text S1 in Supporting Information S1). Second, mesoscale–submesoscale or eddy–edge interactions (McGillicuddy, 2016) could be especially important in the Southern Ocean. Large vertical velocities and fluxes of heat and iron are associated with eddy-generated submesoscale fronts (Siegelman et al., 2020), and chlorophyll filaments around eddies are found by satellite observations (Kahru et al., 2007) and models (Lévy & Klein, 2004; Uchida et al., 2020). However, this submesoscale mechanism is challenging to detect in eddy composites, which blur fine-scale phenomena (McGillicuddy, 2016). Third, the eddies' impact on mixed-layer depth, heat fluxes, and stratification may also have implications for the vertical mixing of oxygen, given its large vertical gradient and faster equilibration with the atmosphere than carbon. Another mechanism by which eddies could influence BGC is by modulating turbulent mixing, for example, by trapping and amplifying near-inertial energy in anticyclones (Voet et al., 2024) or by modulating shear-driven turbulence in marginally stable regimes (Moum et al., 2009). This eddy modulation of turbulence can intensify the diffusive flux of BGC tracers across isopycnals and play an

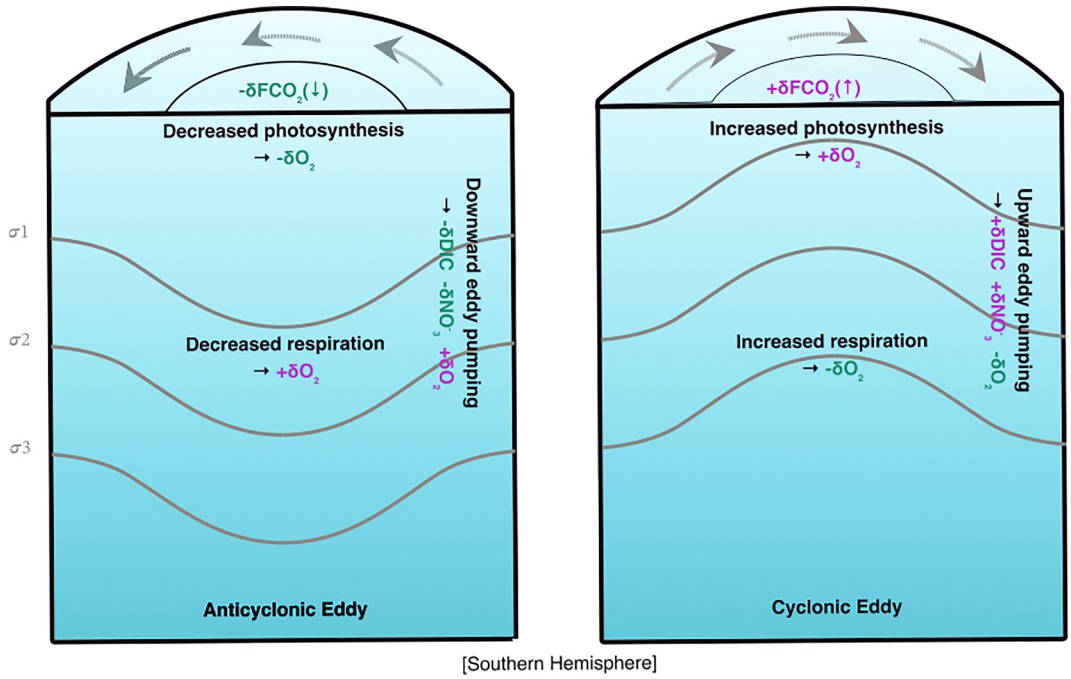

Figure 7. Summarizing schematic: downward eddy pumping in AEs (left) leads to lower DIC, lower nitrate (NO_3^-), and higher dissolved oxygen (O_2) concentrations in the eddy water column. Lower nitrate concentrations then lead to decreased photosynthesis near the surface and, thus, an opposing decrease in dissolved oxygen there. Lower nitrate concentrations lead to decreased respiration at depth and, thus, an increase in dissolved oxygen there. The reduction in surface DIC reduces the CO_2 flux (FCO_2), that is, more oceanic carbon uptake. The opposite is true for CEs (right): upward eddy pumping leads to higher DIC, higher nitrate, and lower dissolved oxygen concentrations in the eddy water column. Higher nitrate concentrations then lead to increased photosynthesis near the surface and, thus, a further increase in dissolved oxygen there. Higher nitrate concentrations lead to increased respiration at depth and, thus, a decrease in dissolved oxygen there. The increase in surface DIC leads to an increase in the CO_2 flux, that is, less oceanic carbon uptake. Note that eddy-induced Ekman pumping offsets the surface effects slightly but is not represented in this schematic.

important role in their mean and seasonal budget balance, for example, for oxygen in the upper equatorial Pacific (Eddebbar et al., 2024). Last, Carranza et al. (2024) and Nicholson et al. (2022) have demonstrated that storms may play a pivotal role in driving carbon outgassing in the Southern Ocean. The interactions between eddies and storms should be further explored, for instance in dedicated mesoscale BGC field process studies using autonomous platforms and high-resolution models.

Finally, the Southern Ocean is a high-nutrient, low-chlorophyll (HNLC) region that is iron and light-limited. Thus, it is unclear if the DIC and oxygen anomalies are directly related to the eddy-induced anomalies in nitrate or indirectly through a correlation with iron, as suggested by Uchida et al. (2019, 2020). Future studies are needed to quantify the mean eddy effect on productivity in this HNLC region. Similarly, other effects, such as eddy-induced heat-driven changes in oxygen and carbon solubility, may also play a role in modulating near-surface biogeochemical distribution and fluxes. Isolating the net effects of these various processes requires higher observational resolution and future model studies.

5. Conclusions

Our co-location of BGC-Argo float profiles with satellite-detected mesoscale eddies has allowed us, for the first time, to observe the anomalous structures of upper-ocean DIC, nitrate, dissolved oxygen, and air–sea CO_2 fluxes in eddies throughout the ice-free Southern Ocean south of 35°S and within subregions. Previous studies had primarily focused on ocean physics or only one BGC tracer, or had been confined to the surface or smaller regions within the Southern Ocean. Our multi-BGC tracer analysis and basin-wide approach provide a comprehensive and mechanistic view of eddy effects on each tracer. The tracers do not all respond similarly, highlighting the need to prioritize comprehensive, accurate sensing of multiple tracers on BGC-Argo floats. Enhanced float coverage

along with more dedicated process studies using BGC-equipped autonomous platforms (e.g., Saildrones and gliders) and high-resolution models may provide renewed opportunities to study these mechanisms in detail.

Our float-based observations of eddy impacts on ocean BGC in the Southern Ocean are summarized in Figure 7. Regional differences in these eddy impacts are largely associated with differences in the vertical background gradients of BGC tracers. The maximum anomalies in all three tracers (DIC, nitrate, and oxygen) were generally deeper in the subduction zone north of the ACC (~500 m) than in the upwelling region in the ACC (~200 m). DIC and nitrate anomalies are larger north of the ACC than in the ACC. In contrast, the magnitude of the oxygen anomalies on depth levels is similar in the two subregions because the different effects (isopycnal heave and along-isopycnal anomalies) cancel each other out. Although the overall impact of eddies on air–sea CO_2 fluxes is weak and not significant (0.02 ± 0.02 Pg C yr^{-1}, i.e., $5 \pm 5\%$), their regional and seasonal differences were more accentuated. We found that at any point in time, ~22% of the ice-free Southern Ocean is covered by eddies (~12% and 10% for AEs and CEs, respectively). Thus, as previous model-based studies have highlighted, resolving eddies in climate models is crucial to obtaining an accurate carbon budget. Our study further highlights the importance of considering eddies and regional and seasonal differences in observing network design.

Conflict of Interest

The authors declare no conflicts of interest relevant to this study.

Data Availability Statement

Meta3.2DT eddies: from Pegliasco et al. (2022), available at https://www.aviso.altimetry.fr/en/data/products/value-added-products/global-mesoscale-eddy-trajectory-product/meta3-2-dt.html. SOCCOM BGC-Argo float data: from Riser et al. (2023), available at http://soccompu.princeton.edu/www/index.html. We use the data snapshot from December 2023 which also includes data from GO-BGC and use the LIAR low-resolution data for estimated parameters. Core-Argo temperature and salinity: from Wong et al. (2020), available at https://www.argo.ucsd.edu/data/. MOBO-DIC: from Keppler et al. (2023a), available at https://www.ncei.noaa.gov/data/oceans/ncei/ocads/metadata/0277099.html. WOA18 nitrate: from Boyer et al. (2018), available at https://www.ncei.noaa.gov/access/world-ocean-atlas-2018/. GOBAI-O2: from Sharp, Fassbender, et al. (2023), available at https://www.ncei.noaa.gov/access/metadata/landing-page/bin/iso?id=gov.noaa.nodc:0259304. Roemmich and Gilson temperature and salinity: from Roemmich and Gilson (2009), available at http://sio-argo.ucsd.edu/RG_Climatology.html. SOM–FFN air–sea CO_2 fluxes, and the parameters to calculate fluxes from pCO_2: We use the latest update of the SOCCOM-weighted SOM–FFN run described in Bushinsky et al. (2019), available at https://www.ncei.noaa.gov/access/ocean-carbon-acidification-data-system/oceans/MPI-SOM_FFN_SOCCOMv2018.html. These runs are variations of the original SOM–FFN runs by Landschützer et al. (2014) and its subsequent versions. Python code for the eddy–float co-location from Tamsitt (2024) also available at https://www.github.com/vtamsitt/eddymatchup.

Acknowledgments
This work was sponsored by NSF's Southern Ocean Carbon and Climate Observations and Modeling (SOCCOM) Project under the NSF awards PLR-1425989 and OPP-1936222, with additional support from NOAA and NASA. The authors also acknowledge support from NSF award OPP-2149501 and OCE-1948599. This study used data from SOCCOM and GO-BGC. Data were collected and made freely available by SOCCOM, funded by the National Science Foundation, Division of Polar Programs (NSF PLR-1425989), supplemented by NASA and by the International Argo Program and the NOAA programs that contribute to it.

References

Argo. (2000). *Argo float data and metadata from global data assembly centre (Argo GDAC)*. SEANOE. https://doi.org/10.17882/42182

Beal, L. M., De Ruijter, W. P. M., Biastoch, A., Zahn, R., Cronin, M., Hermes, J., et al. (2011). On the role of the Agulhas System in ocean circulation and climate. *Nature*, *472*(7344), 429–436. https://doi.org/10.1038/nature09983

Bindoff, N. L., & Mcdougall, T. J. (1994). Diagnosing climate change and ocean ventilation using hydrographic data. *Journal of Physical Oceanography*, *24*(6), 1137–1152. (Publisher: American Meteorological Society Section: Journal of Physical Oceanography). https://doi.org/10.1175/1520-0485(1994)024⟨1137:DCCAOV⟩2.0.CO;2

Boyer, T. P., Garcia, H., Locarnini, R., Zweng, M., Mishonov, A. V., Reagan, J., et al. (2018). World Ocean Atlas 2018 [Dataset]. *NOAA National Centers for Environmental Information*. Retrieved from https://www.ncei.noaa.gov/access/metadata/landing-page/bin/iso?id=gov.noaa.nodc:NCEI-WOA18

Bushinsky, S. M., Gray, A. R., Johnson, K. S., & Sarmiento, J. L. (2017). Oxygen in the Southern Ocean from Argo floats: Determination of processes driving air-sea fluxes. *Journal of Geophysical Research: Oceans*, *122*(11), 8661–8682. https://doi.org/10.1002/2017JC012923

Bushinsky, S. M., Landschützer, P., Rödenbeck, C., Gray, A. R., Baker, D., Mazloff, M. R., et al. (2019). Reassessing Southern Ocean air-sea CO_2 flux estimates with the addition of biogeochemical float observations. *Global Biogeochemical Cycles*, *33*(11), 1370–1388. https://doi.org/10.1029/2019GB006176

Carranza, M. M., Long, M. C., Di Luca, A., Fassbender, A. J., Johnson, K. S., Takeshita, Y., et al. (2024). Extratropical storms induce carbon outgassing over the Southern Ocean. *npj Climate and Atmospheric Science*, *7*(1), 1–16. https://doi.org/10.1038/s41612-024-00657-7

Carter, B. R., Feely, R. A., Williams, N. L., Dickson, A. G., Fong, M. B., & Takeshita, Y. (2018). Updated methods for global locally interpolated estimation of alkalinity, pH, and nitrate. *Limnology and Oceanography: Methods*, *16*(2), 119–131. https://doi.org/10.1002/lom3.10232

Chaigneau, A., Eldin, G., & Dewitte, B. (2009). Eddy activity in the four major upwelling systems from satellite altimetry (1992–2007). *Progress in Oceanography*, *83*(1–4), 117–123. https://doi.org/10.1016/j.pocean.2009.07.012

Chaigneau, A., Le Texier, M., Eldin, G., Grados, C., & Pizarro, O. (2011). Vertical structure of mesoscale eddies in the eastern South Pacific Ocean: A composite analysis from altimetry and Argo profiling floats. *Journal of Geophysical Research*, *116*(C11). https://doi.org/10.1029/2011JC007134

Chelton, D. B., Schlax, M. G., & Samelson, R. M. (2011). Global observations of nonlinear mesoscale eddies. *Progress in Oceanography*, *91*(2), 167–216. https://doi.org/10.1016/j.pocean.2011.01.002

Davis, R. E. (1991). Observing the general circulation with floats. *Deep-Sea Research, Part A: Oceanographic Research Papers*, *38*, S531–S571. https://doi.org/10.1016/S0198-0149(12)80023-9

Dawson, H. R. S., Strutton, P. G., & Gaube, P. (2018). The unusual surface chlorophyll signatures of Southern Ocean eddies. *Journal of Geophysical Research: Oceans*, *123*(9), 6053–6069. https://doi.org/10.1029/2017JC013628

Doddridge, E. W., & Marshall, D. P. (2018). Implications of eddy cancellation for nutrient distribution within subtropical gyres. *Journal of Geophysical Research: Oceans*, *123*(9), 6720–6735. https://doi.org/10.1029/2018JC013842

Dove, L. A., Thompson, A. F., Balwada, D., & Gray, A. R. (2021). Observational evidence of ventilation hotspots in the Southern Ocean. *Journal of Geophysical Research: Oceans*, *126*(7), e2021JC017178. https://doi.org/10.1029/2021JC017178

Dufois, F., Hardman-Mountford, N. J., Greenwood, J., Richardson, A. J., Feng, M., Herbette, S., & Matear, R. (2014). Impact of eddies on surface chlorophyll in the South Indian Ocean. *Journal of Geophysical Research: Oceans*, *119*(11), 8061–8077. https://doi.org/10.1002/2014JC010164

Eddebbar, Y. A., Whitt, D. B., Verdy, A., Mazloff, M. R., Subramanian, A. C., & Long, M. C. (2024). Eddy-mediated turbulent mixing of oxygen in the equatorial Pacific. *Journal of Geophysical Research: Oceans*, *129*(3), e2023JC020588. https://doi.org/10.1029/2023JC020588

Fay, A. R., & McKinley, G. A. (2014). Global open-ocean biomes: Mean and temporal variability. *Earth System Science Data*, *6*(2), 273–284. https://doi.org/10.5194/essd-6-273-2014

Freeland, H., Rhines, P., & Rossby, T. (1975). Statistical observations of the trajectories of neutrally buoyant floats in the North Atlantic. *Journal of Marine Research*, *33*(3).

Frenger, I., Muennich, M., Gruber, N., & Knutti, R. (2015). Southern Ocean eddy phenomenology. *Journal of Geophysical Research: Oceans*, *120*(11), 7413–7449. https://doi.org/10.1002/2015JC011047

Frenger, I., Münnich, M., & Gruber, N. (2018). Imprint of Southern Ocean mesoscale eddies on chlorophyll. *Biogeosciences*, *15*(15), 4781–4798. https://doi.org/10.5194/bg-15-4781-2018

Friedlingstein, P., O'Sullivan, M., Jones, M. W., Andrew, R. M., Bakker, D. C. E., Hauck, J., et al. (2023). Global carbon budget 2023. *Earth System Science Data*, *15*(12), 5301–5369. (Publisher: Copernicus GmbH). https://doi.org/10.5194/essd-15-5301-2023

Gaube, P., Chelton, D. B., Samelson, R. M., Schlax, M. G., & O'Neill, L. W. (2015). Satellite observations of mesoscale eddy-induced Ekman pumping. *Journal of Physical Oceanography*, *45*(1), 104–132. https://doi.org/10.1175/JPO-D-14-0032.1

Gaube, P., McGillicuddy, D. J., Jr., Chelton, D. B., Behrenfeld, M. J., & Strutton, P. G. (2014). Regional variations in the influence of mesoscale eddies on near-surface chlorophyll. *Journal of Geophysical Research: Oceans*, *119*(12), 8195–8220. https://doi.org/10.1002/2014JC010111

Gray, A. R. (2024). The four-dimensional carbon cycle of the Southern Ocean. *Annual Review of Marine Science*, *16*(1), 163–190. https://doi.org/10.1146/annurev-marine-041923-104057

Gray, A. R., Johnson, K. S., Bushinsky, S. M., Riser, S. C., Russell, J. L., Talley, L. D., et al. (2018). Autonomous biogeochemical floats detect significant carbon dioxide outgassing in the high-latitude Southern Ocean. *Geophysical Research Letters*, *45*(45), 9049–9057. https://doi.org/10.1029/2018GL078013

Gregor, L., & Gruber, N. (2021). OceanSODA-ETHZ: A global gridded data set of the surface ocean carbonate system for seasonal to decadal studies of ocean acidification. *Earth System Science Data*, *13*(2), 777–808. https://doi.org/10.5194/essd-13-777-2021

Gruber, N. (2011). Warming up, turning sour, losing breath: Ocean biogeochemistry under global change. *Philosophical Transactions of the Royal Society A: Mathematical, Physical & Engineering Sciences*, *369*(1943), 1980–1996. https://doi.org/10.1098/rsta.2011.0003

Gruber, N., Lachkar, Z., Frenzel, H., Marchesiello, P., Münnich, M., McWilliams, J. C., et al. (2011). Eddy-induced reduction of biological production in Eastern Boundary Upwelling Systems. *Nature Geoscience*, *4*(11), 787–792. https://doi.org/10.1038/ngeo1273

Gruber, N., Landschützer, P., & Lovenduski, N. S. (2019). The variable Southern Ocean carbon sink. *Annual Review of Marine Science*, *11*(1), 159–186. https://doi.org/10.1146/annurev-marine-121916-063407

Harrison, C. S., Long, M. C., Lovenduski, N. S., & Moore, J. K. (2018). Mesoscale effects on carbon export: A global perspective. *Global Biogeochemical Cycles*, *32*(4), 680–703. https://doi.org/10.1002/2017GB005751

Henson, S. A., Laufkötter, C., Leung, S., Giering, S. L. C., Palevsky, H. I., & Cavan, E. L. (2022). Uncertain response of ocean biological carbon export in a changing world. *Nature Geoscience*, *15*(4), 248–254. https://doi.org/10.1038/s41561-022-00927-0

Hogg, A. M., Meredith, M. P., Chambers, D. P., Abrahamsen, E. P., Hughes, C. W., & Morrison, A. K. (2015). Recent trends in the Southern Ocean eddy field. *Journal of Geophysical Research: Oceans*, *120*(1), 257–267. https://doi.org/10.1002/2014JC010470

Ito, T., Woloszyn, M., & Mazloff, M. (2010). Anthropogenic carbon dioxide transport in the Southern Ocean driven by Ekman flow. *Nature*, *463*(7277), 80–83. https://doi.org/10.1038/nature08687

Jersild, A., Delawalla, S., & Ito, T. (2021). Mesoscale eddies regulate seasonal iron supply and carbon drawdown in the Drake Passage. *Geophysical Research Letters*, *48*(24), e2021GL096020. https://doi.org/10.1029/2021GL096020

Jin, Y., Keeling, R. F., Stephens, B. B., Long, M. C., Patra, P. K., Rödenbeck, C., et al. (2024). Improved atmospheric constraints on Southern Ocean CO_2 exchange. *Proceedings of the National Academy of Sciences of the United States of America*, *121*(6), e2309333121. https://doi.org/10.1073/pnas.2309333121

Kahru, M., Mitchell, B. G., Gille, S. T., Hewes, C. D., & Holm-Hansen, O. (2007). Eddies enhance biological production in the Weddell-Scotia Confluence of the Southern Ocean. *Geophysical Research Letters*, *34*(14). https://doi.org/10.1029/2007GL030430

Karstensen, J., Schütte, F., Pietri, A., Krahmann, G., Fiedler, B., Grundle, D., et al. (2017). Upwelling and isolation in oxygen-depleted anticyclonic modewater eddies and implications for nitrate cycling. *Biogeosciences*, *14*(8), 2167–2181. https://doi.org/10.5194/bg-14-2167-2017

Keppler, L., Cravatte, S., Chaigneau, A., Pegliasco, C., Gourdeau, L., & Singh, A. (2018). Observed characteristics and vertical structure of mesoscale eddies in the Southwest Tropical Pacific. *Journal of Geophysical Research-Oceans*, *123*(4), 2731–2756. https://doi.org/10.1002/2017JC013712

Keppler, L., & Landschützer, P. (2019). Regional wind variability modulates the Southern Ocean carbon sink. *Scientific Reports*, *9*(1), 1–10. https://doi.org/10.1038/s41598-019-43826-y

Keppler, L., Landschützer, P., Gruber, N., Lauvset, S. K., & Stemmler, I. (2020). Seasonal carbon dynamics in the near-global ocean. *Global Biogeochemical Cycles*, *34*(12), e2020GB006571. https://doi.org/10.1029/2020GB006571

Keppler, L., Landschützer, P., Lauvset, S. K., & Gruber, N. (2023a). Mapped Observation-Based Oceanic Dissolved Inorganic Carbon monthly fields from 2004 through 2019 (MOBO-DIC2004-2019) [Dataset]. *NOAA National Centers for Environmental Information*. NCEI Accession 0277099. Retrieved from https://www.ncei.noaa.gov/data/oceans/ncei/ocads/metadata/0277099.html

Keppler, L., Landschützer, P., Lauvset, S. K., & Gruber, N. (2023b). Recent trends and variability in the oceanic storage of dissolved inorganic carbon. *Global Biogeochemical Cycles*, *37*(5), e2022GB007677. https://doi.org/10.1029/2022GB007677

Kim, Y. S., & Orsi, A. H. (2014). On the variability of Antarctic Circumpolar Current fronts inferred from 1992–2011 altimetry. *Journal of Physical Oceanography*, *44*(12), 3054–3071. (Publisher: American Meteorological Society Section: Journal of Physical Oceanography). https://doi.org/10.1175/JPO-D-13-0217.1

Köhn, E. E., Münnich, M., Vogt, M., Desmet, F., & Gruber, N. (2022). Strong habitat compression by extreme shoaling events of hypoxic waters in the Eastern Pacific. *Journal of Geophysical Research: Oceans*, *127*(6), e2022JC018429. https://doi.org/10.1029/2022JC018429

Landschützer, P., Gruber, N., & Bakker, D. C. E. (2016). Decadal variations and trends of the global ocean carbon sink. *Global Biogeochemical Cycles*, *30*(10), 1396–1417. https://doi.org/10.1002/2015GB005359

Landschützer, P., Gruber, N., Bakker, D. C. E., & Schuster, U. (2014). Recent variability of the global ocean carbon sink. *Global Biogeochemical Cycles*, *28*(9), 927–949. https://doi.org/10.1002/2014GB004853

Landschützer, P., Gruber, N., Bakker, D. C. E., Schuster, U., Nakaoka, S., Payne, M. R., et al. (2013). A neural network-based estimate of the seasonal to inter-annual variability of the Atlantic Ocean carbon sink. *Biogeosciences*, *10*(11), 7793–7815. https://doi.org/10.5194/bg-10-7793-2013

Landschützer, P., Gruber, N., Haumann, A., Rödenbeck, C., Bakker, D. C. E., van Heuven, S., et al. (2015). The reinvigoration of the Southern Ocean carbon sink. *Science*, *349*(6253), 1221–1224. https://doi.org/10.1126/science.aab2620

Langlais, C. E., Lenton, A., Matear, R., Monselesan, D., Legresy, B., Cougnon, E., & Rintoul, S. (2017). Stationary Rossby waves dominate subduction of anthropogenic carbon in the Southern Ocean. *Scientific Reports*, *7*(1), 17076. https://doi.org/10.1038/s41598-017-17292-3

Laxenaire, R., Speich, S., Blanke, B., Chaigneau, A., Pegliasco, C., & Stegner, A. (2018). Anticyclonic eddies connecting the Western Boundaries of Indian and Atlantic oceans. *Journal of Geophysical Research: Oceans*, *123*(11), 7651–7677. https://doi.org/10.1029/2018JC014270

Lévy, M., & Klein, P. (2004). Does the low frequency variability of mesoscale dynamics explain a part of the phytoplankton and zooplankton spectral variability? *Proceedings of the Royal Society of London. Series A: Mathematical, Physical and Engineering Sciences*, *460*(2046), 1673–1687. https://doi.org/10.1098/rspa.2003.1219

Liu, Q., Liu, Y., & Li, X. (2023). Characteristics of surface physical and biogeochemical parameters within mesoscale eddies in the Southern Ocean. *Biogeosciences*, *20*(23), 4857–4874. https://doi.org/10.5194/bg-20-4857-2023

Long, M. C., Stephens, B. B., McKain, K., Sweeney, C., Keeling, R. F., Kort, E. A., et al. (2021). Strong Southern Ocean carbon uptake evident in airborne observations. *Science*, *374*(6572), 1275–1280. https://doi.org/10.1126/science.abi4355

Martínez-Moreno, J., Hogg, A. M., & England, M. H. (2022). Climatology, seasonality, and trends of spatially coherent ocean eddies. *Journal of Geophysical Research: Oceans*, *127*(7), e2021JC017453. https://doi.org/10.1029/2021JC017453

Mason, E., Pascual, A., & McWilliams, J. C. (2014). A new sea surface height–based code for oceanic mesoscale eddy tracking. *Journal of Atmospheric and Oceanic Technology*, *31*(5), 1181–1188. https://doi.org/10.1175/JTECH-D-14-00019.1

Maurer, T. L., Plant, J. N., & Johnson, K. S. (2021). Delayed-mode quality control of oxygen, nitrate, and pH data on SOCCOM biogeochemical profiling floats. *Frontiers in Marine Science*, *8*. https://doi.org/10.3389/fmars.2021.683207

McGillicuddy, D. J. (2016). Mechanisms of physical-biological-biogeochemical interaction at the oceanic mesoscale. *Annual Review of Marine Science*, *8*(1), 125–159. https://doi.org/10.1146/annurev-marine-010814-015606

McGillicuddy, D. J., Anderson, L. A., Bates, N. R., Bibby, T., Buesseler, K. O., Carlson, C. A., et al. (2007). Eddy/wind interactions stimulate extraordinary mid-ocean plankton blooms. *Science*, *316*(5827), 1021–1026. https://doi.org/10.1126/science.1136256

McGillicuddy, D. J., Jr., Anderson, L. A., Doney, S. C., & Maltrud, M. E. (2003). Eddy-driven sources and sinks of nutrients in the upper ocean: Results from a 0.1° resolution model of the North Atlantic. *Global Biogeochemical Cycles*, *17*(2). https://doi.org/10.1029/2002GB001987

Meredith, M. P., Meijers, A. S., Naveira Garabato, A. C., Brown, P. J., Venables, H. J., Abrahamsen, E. P., et al. (2015). Circulation, retention, and mixing of waters within the Weddell-Scotia Confluence, Southern Ocean: The role of stratified Taylor columns. *Journal of Geophysical Research: Oceans*, *120*(1), 547–562. https://doi.org/10.1002/2014JC010462

Metzl, N., Fin, J., Lo Monaco, C., Mignon, C., Alliouane, S., Antoine, D., et al. (2024). A synthesis of ocean total alkalinity and dissolved inorganic carbon measurements from 1993 to 2022: The SNAPO-CO2-v1 dataset. *Earth System Science Data*, *16*(1), 89–120. https://doi.org/10.5194/essd-16-89-2024

Moum, J. N., Lien, R.-C., Perlin, A., Nash, J. D., Gregg, M. C., & Wiles, P. J. (2009). Sea surface cooling at the Equator by subsurface mixing in tropical instability waves. *Nature Geoscience*, *2*(11), 761–765. https://doi.org/10.1038/ngeo657

Nicholson, S.-A., Whitt, D. B., Fer, I., du Plessis, M. D., Lebéhot, A. D., Swart, S., et al. (2022). Storms drive outgassing of CO_2 in the subpolar Southern Ocean. *Nature Communications*, *13*(1), 158. https://doi.org/10.1038/s41467-021-27780-w

Orsi, A. H., Whitworth, T., & Nowlin, W. D. (1995). On the meridional extent and fronts of the Antarctic Circumpolar Current. *Deep-Sea Research Part I Oceanographic Research Papers*, *42*(5), 641–673. https://doi.org/10.1016/0967-0637(95)00021-W

Patara, L., Böning, C. W., & Biastoch, A. (2016). Variability and trends in Southern Ocean eddy activity in 1/12° ocean model simulations. *Geophysical Research Letters*, *43*(9), 4517–4523. https://doi.org/10.1002/2016GL069026

Patel, R. S., Llort, J., Strutton, P. G., Phillips, H. E., Moreau, S., Conde Pardo, P., & Lenton, A. (2020). The biogeochemical structure of Southern Ocean mesoscale eddies. *Journal of Geophysical Research: Oceans*, *125*(8), e2020JC016115. https://doi.org/10.1029/2020JC016115

Pegliasco, C., Chaigneau, A., & Morrow, R. (2015). Main eddy vertical structures observed in the four major Eastern Boundary Upwelling Systems. *Journal of Geophysical Research: Oceans*, *120*(9), 6008–6033. https://doi.org/10.1002/2015JC010950

Pegliasco, C., Delepoulle, A., Mason, E., Morrow, R., Faugère, Y., & Dibarboure, G. (2022). META3.1exp: A new global mesoscale eddy trajectory Atlas derived from altimetry. *Earth System Science Data*, *14*(3), 1087–1107. https://doi.org/10.5194/essd-14-1087-2022

Prend, C. J., Gille, S. T., Talley, L. D., Mitchell, B. G., Rosso, I., & Mazloff, M. R. (2019). Physical drivers of phytoplankton bloom initiation in the Southern Ocean's Scotia Sea. *Journal of Geophysical Research: Oceans*, *124*(8), 5811–5826. https://doi.org/10.1029/2019JC015162

Prend, C. J., Gray, A. R., Talley, L. D., Gille, S. T., Haumann, F. A., Johnson, K. S., et al. (2022). Indo-Pacific sector dominates southern ocean carbon outgassing. *Global Biogeochemical Cycles*, *36*(7), e2021GB007226. https://doi.org/10.1029/2021GB007226

Prend, C. J., Keerthi, M. G., Lévy, M., Aumont, O., Gille, S. T., & Talley, L. D. (2022). Sub-seasonal forcing drives year-to-year variations of Southern Ocean primary productivity. *Global Biogeochemical Cycles*, *36*(7), e2022GB007329. https://doi.org/10.1029/2022GB007329

Resplandy, L., Lévy, M., & McGillicuddy, D. J., Jr. (2019). Effects of eddy-driven subduction on ocean biological carbon pump. *Global Biogeochemical Cycles*, *33*(8), 1071–1084. https://doi.org/10.1029/2018GB006125

Riser, S. C., Talley, L. D., Wijffels, S. E., Nicholson, D., Purkey, S., Takeshita, Y., et al. (2023). SOCCOM and GO-BGC float data—snapshot 2023-04-26. In *Southern ocean carbon and climate observations and modeling (SOCCOM) and global ocean biogeochemistry (GO-BGC) biogeochemical-argo float data archive*. UC San Diego Library Digital Collections. https://doi.org/10.6075/J0542NS9

Roemmich, D., & Gilson, J. (2009). The 2004–2008 mean and annual cycle of temperature, salinity, and steric height in the global ocean from the Argo program. *Progress in Oceanography*, *82*(2), 81–100. https://doi.org/10.1016/j.pocean.2009.03.004

Rohr, T., Harrison, C., Long, M. C., Gaube, P., & Doney, S. C. (2020). The simulated biological response to Southern Ocean eddies via biological rate modification and physical transport. *Global Biogeochemical Cycles*, *34*(6), e2019GB006385. https://doi.org/10.1029/2019GB006385

Roman-Stork, H. L., Byrne, D. A., & Leuliette, E. W. (2023). MESI: A multiparameter eddy significance Index. *Earth and Space Science*, *10*(2), e2022EA002583. https://doi.org/10.1029/2022EA002583

Rosso, I., Mazloff, M. R., Talley, L. D., Purkey, S. G., Freeman, N. M., & Maze, G. (2020). Water mass and biogeochemical variability in the Kerguelen sector of the Southern Ocean: A machine learning approach for a mixing hot spot. *Journal of Geophysical Research: Oceans*, *125*(3), e2019JC015877. https://doi.org/10.1029/2019JC015877

Sarmiento, J. L., & Gruber, N. (2006). Carbon cycle, CO_2, and climate; the anthropogenic perturbation. In *Ocean biogeochemical dynamics* (pp. 399–417). Princeton University Press.

Sarmiento, J. L., Gruber, N., Brzezinski, M. A., & Dunne, J. P. (2004). High-latitude controls of thermocline nutrients and low latitude biological productivity. *Nature*, *427*(6969), 56–60. https://doi.org/10.1038/nature02127

Sarmiento, J. L., Johnson, K. S., Arteaga, L. A., Bushinsky, S. M., Cullen, H. M., Gray, A. R., et al. (2023). The Southern Ocean carbon and climate observations and modeling (SOCCOM) project: A review. *Progress in Oceanography*, *219*, 103130. https://doi.org/10.1016/j.pocean.2023.103130

Schütte, F., Karstensen, J., Krahmann, G., Hauss, H., Fiedler, B., Brandt, P., et al. (2016). Characterization of "dead-zone" eddies in the eastern tropical North Atlantic. *Biogeosciences*, *13*(20), 5865–5881. https://doi.org/10.5194/bg-13-5865-2016

Sharp, J. D., Fassbender, A. J., Carter, B. R., Johnson, G. C., Schultz, C., & Dunne, J. P. (2023). GOBAI-O_2: Temporally and spatially resolved fields of ocean interior dissolved oxygen over nearly two decades. *Earth System Science Data Discussions*, 1–46. https://doi.org/10.5194/essd-2022-308

Sharp, J. D., Pierrot, D., Humphreys, M. P., Epitalon, J.-M., Orr, J. C., Lewis, E. R., & Wallace, D. W. (2023). *CO2SYSv3 for MATLAB*. Zenodo. https://doi.org/10.5281/zenodo.7552554

Siegelman, L., Klein, P., Rivière, P., Thompson, A. F., Torres, H. S., Flexas, M., & Menemenlis, D. (2020). Enhanced upward heat transport at deep submesoscale ocean fronts. *Nature Geoscience*, *13*(1), 50–55. https://doi.org/10.1038/s41561-019-0489-1

Stern, M. E. (1965). Interaction of a uniform wind stress with a geostrophic vortex. *Deep-Sea Research and Oceanographic Abstracts*, *12*(3), 355–367. https://doi.org/10.1016/0011-7471(65)90007-0

Su, J., Strutton, P. G., & Schallenberg, C. (2021). The subsurface biological structure of Southern Ocean eddies revealed by BGC-Argo floats. *Journal of Marine Systems*, *220*, 103569. https://doi.org/10.1016/j.jmarsys.2021.103569

Swierczek, S., Mazloff, M. R., Morzfeld, M., & Russell, J. L. (2021). The effect of resolution on vertical heat and carbon transports in a regional ocean circulation model of the Argentine Basin. *Journal of Geophysical Research: Oceans*, *126*(7), e2021JC017235. https://doi.org/10.1029/2021JC017235

Talley, L., Pickard, G. L., Emery, W. J., & Swift, J. H. (2011). *Descriptive physical oceanography*. Elsevier. https://doi.org/10.1016/C2009-0-24322-4

Talley, L., Rosso, I., Kamenkovich, I., Mazloff, M. R., Wang, J., Boss, E., et al. (2019). Southern Ocean biogeochemical float deployment strategy, with example from the Greenwich Meridian line (GO-SHIP A12). *Journal of Geophysical Research: Oceans*, *124*(1), 403–431. https://doi.org/10.1029/2018JC014059

Tamsitt, V. (2024). Eddy match up code. *Zenodo*. https://doi.org/10.5281/zenodo.14165856

Uchida, T., Balwada, D., Abernathey, P., A. McKinley, G., K. Smith, S., Lévy, M., & Lévy, M. (2020). Vertical eddy iron fluxes support primary production in the open Southern Ocean. *Nature Communications*, *11*(1), 1125. https://doi.org/10.1038/s41467-020-14955-0

Uchida, T., Balwada, D., Abernathey, R., Prend, C. J., Boss, E., & Gille, S. T. (2019). Southern Ocean phytoplankton blooms observed by biogeochemical floats. *Journal of Geophysical Research: Oceans*, *124*(11), 7328–7343. https://doi.org/10.1029/2019JC015355

Vilela-Silva, F., Bindoff, N. L., Phillips, H. E., Rintoul, S. R., & Nikurashin, M. (2024). The impact of an Antarctic Circumpolar Current meander on air-sea interaction and water subduction. *Journal of Geophysical Research: Oceans*, *129*(7), e2023JC020701. https://doi.org/10.1029/2023JC020701

Voet, G., Waterhouse, A., Savage, A., Kunze, E., MacKinnon, J., Alford, M., et al. (2024). Near-inertial energy variability in a strong mesoscale eddy field in the Iceland basin. *Oceanography*. https://doi.org/10.5670/oceanog.2024.302

Wang, T., Gille, S. T., Mazloff, M. R., Zilberman, N. V., & Du, Y. (2020). Eddy-induced acceleration of Argo floats. *Journal of Geophysical Research: Oceans*, *125*(10), e2019JC016042. https://doi.org/10.1029/2019JC016042

Williams, N. L., Juranek, L. W., Feely, R. A., Johnson, K. S., Sarmiento, J. L., Talley, L. D., et al. (2017). Calculating surface ocean pCO_2 from biogeochemical Argo floats equipped with pH: An uncertainty analysis. *Global Biogeochemical Cycles*, *31*(3), 591–604. https://doi.org/10.1002/2016GB005541

Wong, A. P. S., Wijffels, S. E., Riser, S. C., Pouliquen, S., Hosoda, S., Roemmich, D., et al. (2020). Argo data 1999–2019: Two million temperature-salinity profiles and subsurface velocity observations from a global array of profiling floats. *Frontiers in Marine Science*, *7*. https://doi.org/10.3389/fmars.2020.00700